

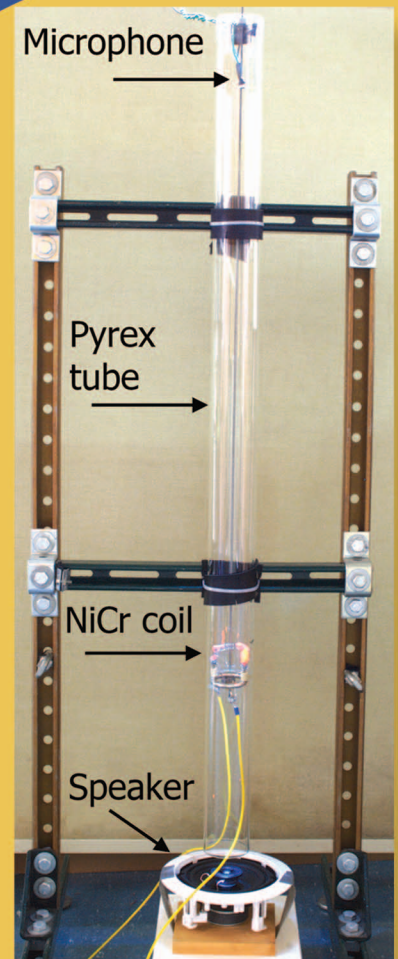
Thermoacoustics and the Rijke Tube

EXPERIMENTS,
IDENTIFICATION,
AND MODELING

JONATHAN P. EPPERLEIN,
BASSAM BAMIEH, and KARL J. ÅSTRÖM

The Rijke tube [1] is a classic experiment that is relatively simple and inexpensive to build in a typical university laboratory. Despite its construction simplicity, it can serve to illustrate a wide variety of mathematical modeling, empirical identification, verification, and feedback control techniques. As such, it is suitable for use in both advanced undergraduate and graduate control laboratory courses.

The Rijke tube also serves as prototypical experiment for research and study of *thermoacoustic phenomena* in which heat transfer and acoustics are dynamically coupled. This experiment is perhaps the simplest illustration of the phenomenon of thermoacoustic instabilities, which typically occur whenever heat is released into gas in underdamped acoustic cavities. The heat release can be due to combustion or solid/gas heat transfer. Under the right conditions, the coupling between the acoustic and heat release dynamics in the cavity becomes unstable. This instability manifests itself as a sustained limit cycle resulting in audible, powerful pressure oscillations. Thermoacoustic instability phenomena are most often encountered in combustors [2], [3], where the resulting powerful pressure waves are undesirable due to the danger of structural damage as well as performance degradations. In this context, they are often referred to as combustion instabilities and are notoriously difficult to model due to the additional complexity of combustion dynamics [4], [5]. One advantage of the Rijke tube is that it generates thermoacoustic instabilities without a combustion process. The absence of combustion renders the mathematical modeling



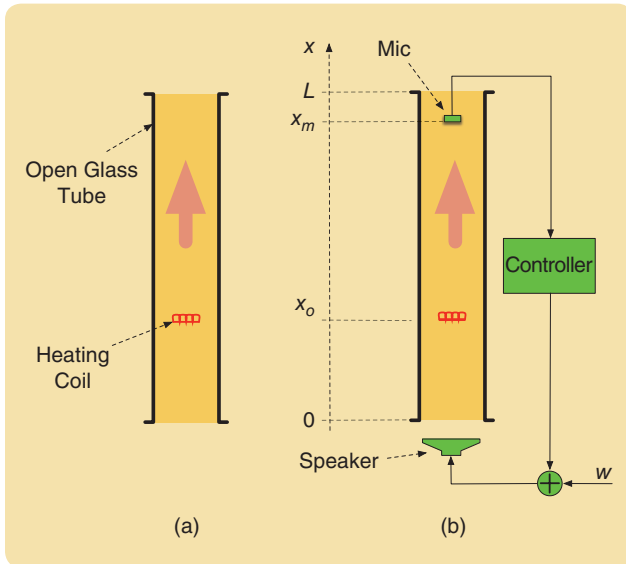


FIGURE 1 (a) The Rijke tube shown with a heating element placed toward the bottom (suspension mechanism for coil not shown). The upward arrow indicates steady air flow caused by the coil's heat. (b) The Rijke tube with a microphone, speaker, and feedback controller. The external signal w is used for closed-loop identification.

and subsequent system analysis problems significantly more tractable, yet many of the identification and feedback control issues involved in combustion instabilities are present in the Rijke tube. Thus, this experiment provides an easily accessible platform within which to explore the myriad issues relevant to thermoacoustic instabilities and their control.

This article aims at introducing the Rijke tube as both an experimental and theoretical platform to explore thermoacoustic dynamics and their control. The first part is an experimental investigation of the dynamics of the Rijke tube using closed-loop identification and model validation. The second part details the derivation of a control-oriented model from the simplified thermoacoustic physics of one-dimensional gas dynamics. This model is examined using linear time-invariant (LTI) system tools such as the root locus and the Nyquist criterion, giving insight into the open-loop instability and the effects of feedback control. The first part is an empirical approach that requires little knowledge of the underlying physics, and it is remarkable that rather useful and predictive models of the system can be obtained with this approach. In the courses at the University of California, Santa Barbara (UCSB), most students who have performed this experiment and subsequent analysis did not start out with any knowledge of thermoacoustic physics. Further insight is obtained by combining the results of the feedback control experiments with the theoretical models developed in the second part. The section on mathematical modeling has been made compact and self-contained and is easily accessible to readers with a control engineering background. This perhaps distinguishes this article from other excellent treatments of the Rijke tube in

the literature (such as [6]–[8] and the review article [9]), in that the self-contained presentation is written for a control engineering audience.

Prior to embarking on the two main components of this article, a brief description of how a typical Rijke tube experiment is conducted, the observations that can be made, and the construction of the apparatus are given.

OBSERVATIONS OF THE RIJKE TUBE AND ITS CONTROL

By way of an introduction, some basic observations that can be quickly made in the laboratory are described. These observations set the stage for the many modeling, identification, and control questions that can be subsequently posed and investigated. Figure 1(a) illustrates the basic operation of the Rijke tube. A heating element (typically a resistive coil) is placed in the bottom third of a vertical open glass tube; for details on the specific setup at UCSB, see “Construction of the Rijke Tube Apparatus.” If the coil is sufficiently hot, a steady upward flow of air is achieved. An increase in the power to the coil causes an increase in the air flow, and at some critical value of this power, the tube begins to emit a loud, steady “hum” like a pipe organ. A decrease in the power to the coil will cause the hum to die out. A measurement of the frequency of that sound, and assuming typical sound velocity in air at room temperature, shows the wavelength to be equal to twice the length of the tube. This is consistent with a half-wavelength standing wave in the tube.

The next step is to experiment with a simple active acoustic feedback scheme. A speaker is placed a slight distance under the tube and is powered by a variable gain amplifier with input from a microphone put near the top of the tube. This is illustrated in Figure 1(b), where the amplifier is referred to as the controller. This arrangement can be thought of as simple proportional feedback. If the power to the coil is made sufficiently high, causing the tube to hum, the effects of the feedback gain can be investigated via experiments. If the sign of the feedback gain is chosen correctly, it is observed that as the gain is increased upward from zero, there is a critical value of the feedback gain that causes the loud hum to quickly disappear. A natural question is whether this represents a stabilization of an unstable process or possibly some form of noise cancellation. A quick check of the control signal (speaker input) reveals that signal to be near zero, indicating that the speaker is indeed stabilizing the thermoacoustic instability rather than canceling the noise produced by it. This simple stabilization scheme allows for closed-loop system identification to be done, from which an empirically determined open-loop transfer function can be obtained.

After stabilization by simple proportional feedback, the next step is the investigation of the gain margin and what happens at high gains. It is observed that with further increase in the feedback gain, the tube begins to emit a

Construction of the Rijke Tube Apparatus

The particular Rijke tube hardware configuration used in the control laboratory at UCSB is described briefly. Details of this basic setup can be easily modified according to other specific laboratory facilities. The basic apparatus used for this experiment (see Figure S1) is composed of the following main components:

- glass tube, length = 4 ft, internal diameter = 3 in (a high aspect ratio is necessary to achieve thermoacoustic instability with only moderate heater power)
- heater coil (resistive Nichrome heater)
- microphone and pre-amplifier (for example, a simple op-amp circuit)
- speaker
- power amplifier (for speaker)
- ac or dc variable power supply (for heater coil).

A data acquisition (DAQ) board and Simulink Real-Time Windows Target are used to collect data. Either a simple op-amp circuit or a Simulink block can be used to realize the variable feedback control gain, with the former option illustrated in Figure S1. The glass tube is vertically mounted to a rigid frame, with the heater coil mounted about one-quarter of the way up from the bottom of the tube. The power supply is used to heat the coil. The microphone is mounted near the top and in the center of the tube's cross section. The microphone signal (ac coupled) is fed via the DAQ board to Simulink, where it is recorded and multiplied with the variable gain. The test signal (used for system

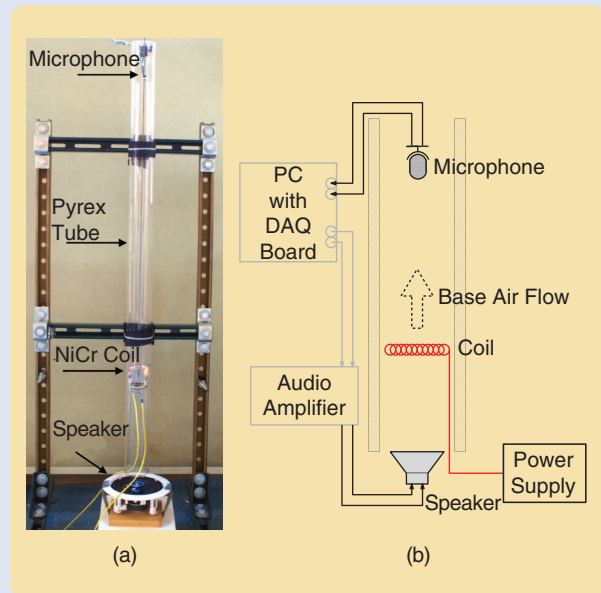


FIGURE S1 A photograph and diagram of the UCSB Rijke tube experimental apparatus.

identification, see Figure 5) is also added there. The generated signal is then routed from the DAQ board to the audio amplifier to the speaker.

loud screeching sound, at a different and higher frequency than the hum observed at the lower gain. A measurement of the screech frequency yields that it is roughly a harmonic of the originally observed hum frequency. Often it will be either the third or fifth harmonic, with other harmonics occurring less often. Exactly which of the harmonics it is depends on the microphone position and is an important feature of the problem that can be later used for the model validation component of the experiment. In summary, the instability at high feedback gains (the screech) occurs due to the right-half plane (RHP) zeros inherent in this system. The open-loop pole locations are determined by the tube's acoustics and are largely independent of speaker and microphone position. However, the open-loop zero locations, which influence the high-gain instability, depend on the actuator and sensor locations.

EMPIRICAL INVESTIGATION OF THE RIJKE TUBE

The experimental exploration of the Rijke tube begins with establishing the conditions for the initial thermoacoustic instability as a function of heater power input. The effects of proportional acoustic feedback are then investigated through initial stabilization and then observing instabilities at high gains. Once a stable system is established, closed-loop identification is performed, and a model from frequency response data is obtained. A root locus analysis of

the identified model is used to explain the basic thermoacoustic instability. Locations of the open-loop poles and zeros of the identified model play an important role in the dynamics, and root locus analysis is used to further validate the model using observations of the high-gain instabilities.

Observing the Thermoacoustic Instability

The initial operation of the Rijke tube is quite simple: the heater coil power supply is turned on and increased slowly. During this process, the upward flow of hot air can be felt by placing a hand slightly over the top of the tube. There is a critical heater power beyond which the tube will begin to hum loudly. The increase in sound level up to saturation occurs in a couple of seconds [see Figure 2(a)]. If the heater power is decreased and then increased again [see Figure 2(a)], a slight hysteresis phenomenon can be observed. The sound [see Figure 2(a)] frequency f is easily measured with an oscilloscope, and using the speed of sound under standard conditions $c = 343$ m/s, its wavelength, $\lambda = c/f$, is approximately equal to twice the length of the tube. This observation is consistent with a half-wavelength standing wave in the tube, which is the fundamental mode of a tube open at both ends, which for the setup used in this article has a frequency of approximately 143 Hz; see Table 1 and "Construction of the Rijke Tube Apparatus." The basic physics of that mode are illustrated in Figure 3.

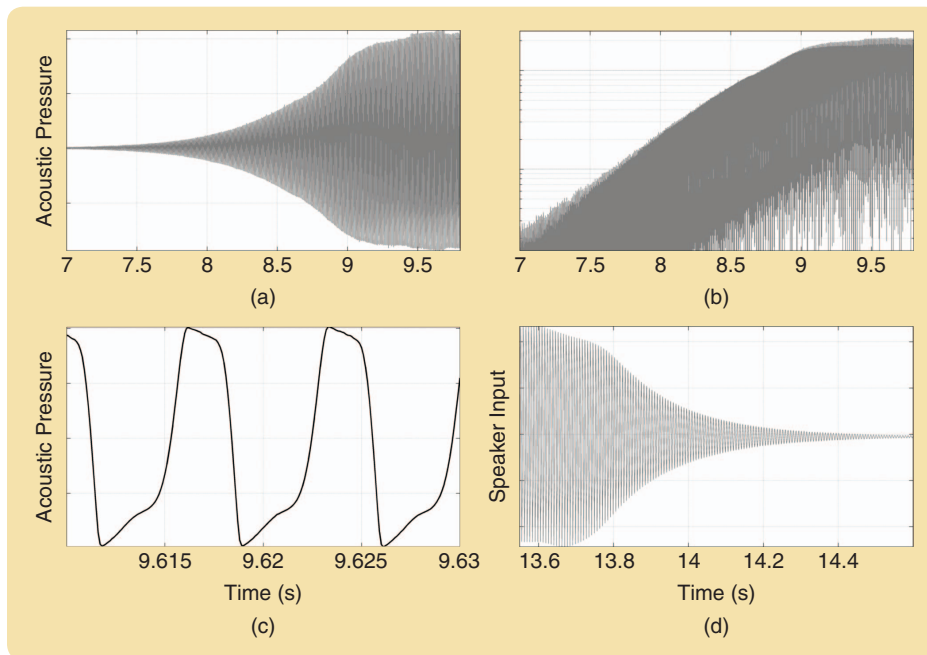


FIGURE 2 A time trace of the (a) microphone signal at the onset of instability showing growth, and then saturation of the limit cycle. Linear growth on a (b) semilog plot of the signal's envelope confirms initial exponential growth of its amplitude. A (c) zoomed-in picture shows the periodic, but nonsymmetric, limit-cycle behavior. With appropriate proportional feedback, the limit cycle is stabilized as this trace of the (d) speaker's input signal shows.

While it is common to assume that every mode has a pressure node exactly at the open end, in reality, the nodes are located slightly outside the tube. This discrepancy can be accounted for by using a tube length $L + 2\Delta L$ in the computations; the end correction ΔL depends on the radius R of the tube and the wavelength λ of the considered mode, but for $\lambda \gg R$ it is approximately independent of λ : $\Delta L \approx 0.61R$ [10]. For the tube considered here, the difference is merely 8 Hz.

TABLE 1 Values of relevant parameters used for computations.

Symbol		Value Used
$\bar{\rho}$	Density	1.2 kg/m ³
\bar{p}	Pressure	10 ⁵ N/m ²
$c = \sqrt{\gamma \frac{\bar{p}}{\bar{\rho}}}$	Speed of sound	343 m/s
c_p	Specific heat capacities	1008 J/(kg K)
c_v		718 J/(kg K)
$\gamma = c_p/c_v$	Adiabatic ratio	1.4
$\bar{\gamma} := \gamma - 1$	—	0.4
$R = c_p - c_v$	Ideal gas constant	290 J/(kg K)
L	Tube length	1.219 m
t_{hr}	Heat release time constant	$\approx 3.5 \cdot 10^{-4}$ s

Proportional Acoustic Feedback

When the microphone, data acquisition (DAQ) board, and speaker are connected as shown in Figures 1(b) and S1, proportional feedback can be applied to the Rijke tube. It is observed that as the gain of the power amplifier is increased, there is a critical gain value K_{min} above which the tube's hum will quickly disappear; see Figure 2(d). This is usually an impressive demonstration of the power of feedback.

Since many students who perform this experiment are not familiar with acoustics, they are often unsure as to what is happening when the tube's hum disappears. They often say that the tube's noise has been "cancelled," probably because of familiarity with noise-canceling headsets. However, the process here is funda-

mentally different. The feedback has *stabilized* the thermoacoustic instability that caused the limit cycle in the first place. To verify the distinction between stabilization and noise cancellation, it is sufficient to observe the control signal into the speaker terminals on an oscilloscope as the critical feedback gain is reached and the hum disappears. The oscilloscope will show that the control signal decays rapidly and hovers around zero as the critical stabilizing feedback gain value is reached; see again Figure 2(d). In contrast, a noise-canceling system would have a persistent nonzero control signal canceling the persistent noise. Interesting phenomena occur at higher gains. There is a critical higher gain value K_{max} above which a new instability is triggered. When that gain is reached, the tube will begin to screech loudly. A measurement of that screech frequency reveals it to be a harmonic of the initial fundamental hum frequency (as depicted in Figure 4). Exactly which harmonic causes the screech will depend on the details of the experimental setup (in the setup used at UCSB it is typically the third or fifth harmonic). This phenomenon is, however, repeatable if the experimental setup, the microphone, speaker, and heater locations, is unchanged. The screech frequency should be noted since it can be predicted from a root locus analysis of the identified system model and therefore can be used to validate that model.

Closed-Loop Identification

In this empirical approach to the Rijke tube, no physical modeling is done. Instead, system identification tools are

used to obtain information about the dynamics. The Rijke tube with the heater on is an unstable system and therefore must be identified while operating in a stabilizing closed loop. Stabilization can be achieved by a proportional controller implemented by a speaker, a microphone, and amplifiers. These components have dynamics that will appear as being lumped with the Rijke tube dynamics, as shown in the conceptual block diagram in Figure 5. However, because they are designed for the human hearing range (20–20,000 Hz), their contribution over the frequencies of interest in this experiment (typically 100–1,000 Hz) will be small. The test signal w is generated externally, in Simulink for example, and then added to the control signal; it is the input for the closed-loop system identification process.

Closed-Loop System Identification

Care needs to be taken when identifying systems in a closed loop, since simply recording the plant input and output and applying open-loop identification techniques, ignoring the fact that the input is the result of feedback, might yield wrong results. In particular, the closed loop system loses the property of consistency, meaning that infinite data will no longer result in an exact identification of the underlying system. The reason is that most identification techniques start from a system model of the form $y(t) = Fu(t) + v(t)$, where v represents measurement noise and F is the transfer function of the system to be identified, and it is assumed that the noise and input are uncorrelated. However, if the system operates in closed loop, the input $u(t)$ is determined from the measured output and hence now correlates with the measurement noise. The simplest work-around, and the one chosen here, is the *indirect method*. As shown in the conceptual block diagram in Figure 5, an exogenous test signal w is added into the loop. The structure of the model then is $y(t) = Tw(t) + v(t)$, but T is the closed-loop transfer function, and w and v are indeed uncorrelated. Its frequency response $T(e^{j\omega})$ can then be identified with any open-loop technique, and the open-loop response $F(e^{j\omega})$ can be recovered by simple algebra. For more background and more sophisticated methods see, for example, [11] and [12]. Here, the closed-loop transfer function from the test signal w (added into the input of the power amplifier) to the microphone output y is

$$T = \frac{KF}{1 - KF}$$

where K is the aggregation of all the gains of the other components (assumed to be independent of frequency) in the loop. Once T is identified, F is obtained by inverting the above relation

$$F = \frac{1}{K} \frac{T}{1 + T}. \quad (1)$$

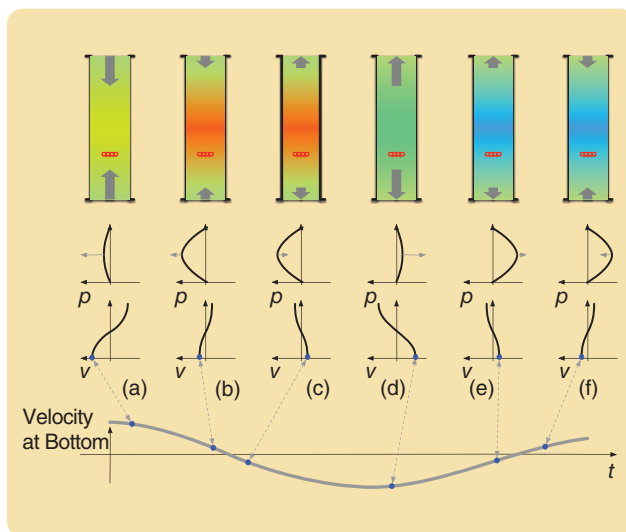


FIGURE 3 A diagram of the fundamental acoustic mode of the Rijke tube showing its half-wave nature. In the top three rows, the spatial waveforms are shown. In the first row, acoustic pressure is shown in color, and the acoustic velocity at the ends is illustrated as arrows. The bottom row depicts one period of the temporal waveform of the velocity at the bottom of the tube. In phase (a), the pressure just started increasing in the center of the tube due to the air rushing in, which in (b) has led to the pressure achieving a maximum at the center, while, simultaneously, the velocity has been decreased by the resulting pressure gradient. In (c), the pressure gradient has inverted the velocity, so that air now starts rushing out of the tube with (d) increasing velocity, until (e) the pressure reaches a minimum in the center and the gradient leads to (f) air being sucked in again, until (a) pressure moves toward its maximum again and the cycle repeats.

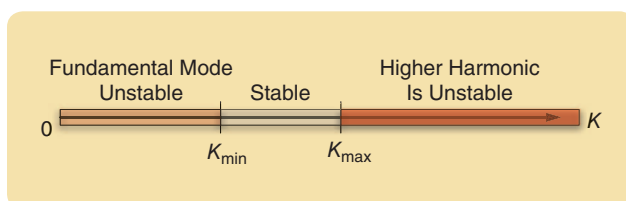


FIGURE 4 A depiction of the effects of proportional feedback on the Rijke tube. A minimum feedback gain K_{\min} is necessary to stabilize the unstable fundamental mode. There is then a critical higher gain K_{\max} , beyond which a higher harmonic mode of the tube becomes unstable, yielding a high-pitched screech.

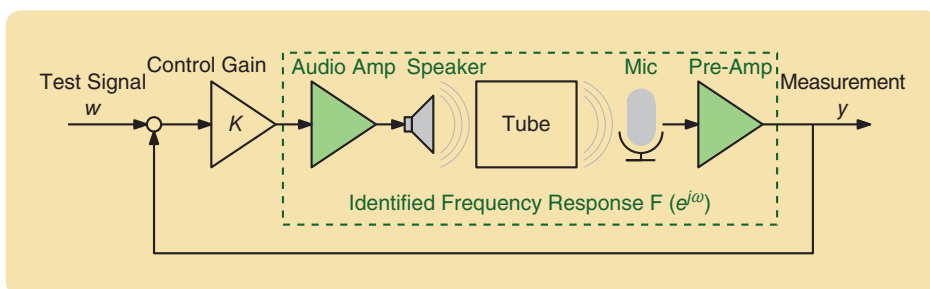


FIGURE 5 An equivalent block diagram of the Rijke tube with acoustic feedback. The speaker, microphone, and pre-amp transfer functions are lumped together with that of the Rijke tube. The controller is simply regarded as a variable gain. The external test signal w is used for closed-loop identification.

It would be very difficult to obtain a value for K , which, for instance, incorporates the unknown conversion factor from pressure to voltage output by the microphone, but the above equation shows that the poles and zeros of F can be identified from those of T without knowing K . In other words, F is identified up to an unknown gain factor $1/K$.

Despite the issues mentioned, the “direct method” of simply applying open-loop techniques to the plant input u and the output y might be a viable alternative in practical applications, in particular when the controller K is very complex or unknown. An external signal w should still be used to ensure rich-enough frequency content in u . For example, in [13] and [14], such methods are applied successfully to the Rijke tube.

Open-Loop Identification Method

The dynamics underlying the Rijke tube are a combination of acoustics and heat transfer and are thus of relatively high order (in fact, they are infinite dimensional). Nonparametric frequency-domain identification schemes are better suited to those types of systems than time-domain based ones since a model order does not have to be selected a priori. Instead, the frequency response $T(e^{j\omega})$ is identified directly, and then a least-squares-based method is used to fit a model of appropriate order over the identified frequency range. Spectral methods (see, for example, [15, Ch. 6]) estimate the frequency response as the ratio of the cross-spectrum $\Phi_{yw}(\omega)$ of output and test signal and the spectrum $\Phi_w(\omega)$ of the test signal. The Matlab System Identification Toolbox [16] offers two implementations of these methods, `spa` and `spafdr`. While both estimate the cross spectrum and input spectrum by applying a smoothing window to what roughly amounts to the discrete Fourier transforms of input and output data, `spa` performs the windowing in the time domain, whereas `spafdr` applies the window in the frequency domain. The expected sharp peaks in the frequency response require fine resolution in frequency; since a narrow frequency-domain window, which is what is required, corresponds to a wide time-domain window, using `spafdr` allows for specifying a small (frequency-domain) window, resulting in a drastic decrease in computation time compared to the large (time-domain) window that would have to be specified to achieve the same resolution using `spa`. (Another important distinction between `spa` and `spafdr` is that the latter allows for frequency-dependent resolution (hence the name), but this feature was not used here). The least-squares fit is then performed using the function `clsfits` from the FREQID Toolbox for Matlab [17].

Test Signal

A test signal should have rich frequency content, while, due to actuator and sensor limitations in physical systems, amplitudes should be kept reasonably small. Popular choices include white noise, Schroeder-phased sinusoids [18], and sine sweeps (also known as chirp signals). After experiments with all three types of signals, sine sweeps, which have been found to be beneficial in the identification of acoustic systems [19], emerged as the most effective choice; all shown data was collected using a sweep over the shown frequency range.

For the identification experiment, the tube is first brought to a hum. Then, the feedback with a stabilizing gain is turned on, and the test signal is added to the feedback signal, as shown in Figure 5. The microphone signal is recorded for the duration of the experiment (the data used here was collected over 120 s), and together with the applied test signal forms an input–output pair, which is all the data needed to obtain a spectral estimate. To minimize the effects of random noise, this procedure is repeated several times, and an average of the estimated frequency responses is formed. Figure 6 shows an averaged closed-loop

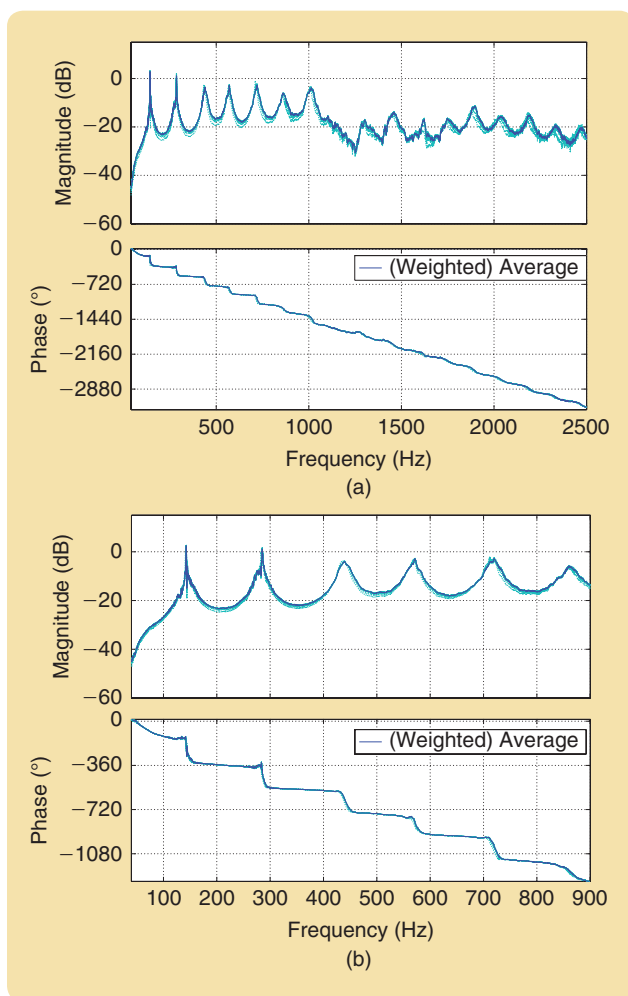


FIGURE 6 The closed-loop frequency response obtained with a sine sweep over the range of (a) 0–2.5 kHz and (b) 0–900 Hz. The response below 20 Hz, which is outside the audible range, and above 1 kHz is likely dominated by microphone and speaker distortions. The range 0–1 kHz, however, exhibits typical wave-like dynamics with resonances occurring at multiples of the fundamental frequency. Note that here and in all Bode plots that follow, a linear frequency axis is used to emphasize the pattern of a fundamental frequency with harmonics.

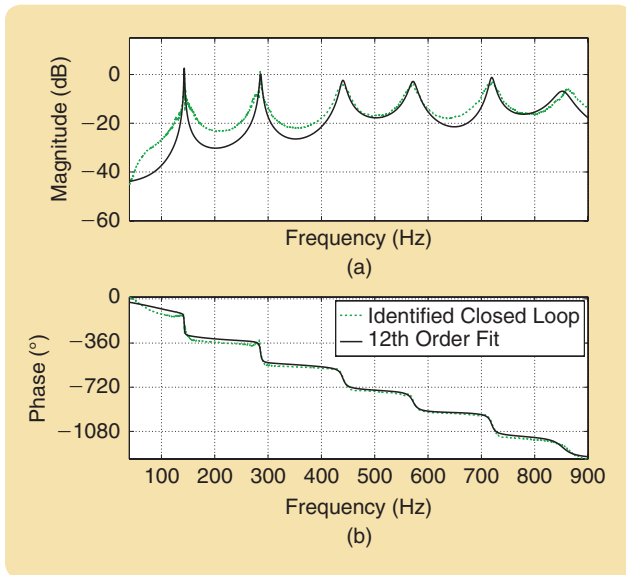


FIGURE 7 The closed-loop frequency response obtained by a non-parametric spectral estimation and a 12th-order least-squares fit. Note that, due to the log y-scale, the seemingly large deviations in the ranges between the peaks are actually very small.

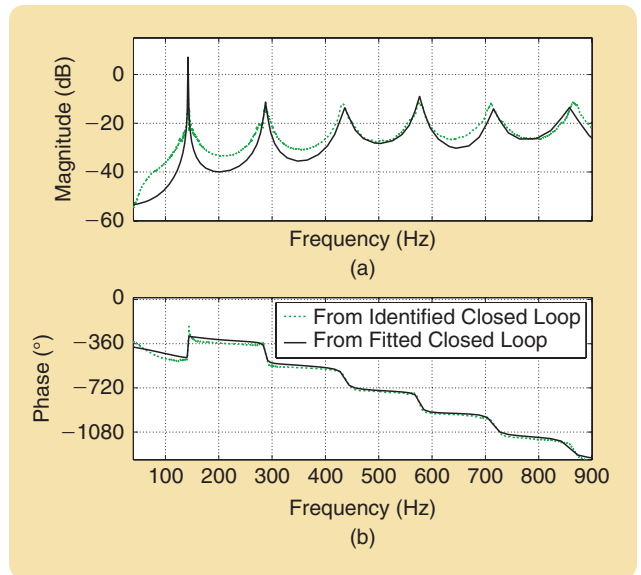


FIGURE 8 Open-loop frequency responses, obtained by applying (1) to the identified closed-loop response at every frequency (green) or to the fitted closed-loop response (black).

frequency response along with the individual experiments. This response, with several very lightly damped modes at integer multiples of a fundamental frequency, has the signature of wave-like dynamics. The fundamental frequency corresponds very closely to the frequency of the hum observed in the nonstabilized Rijke tube.

To perform the least-squares fit of a finite-dimensional transfer function model for T to the estimated frequency response, a value for the model order needs to be selected. Figure 7 shows a 12th-order transfer function fit, which nicely captures the first six harmonics in the frequency response.

To obtain the transfer function F , which is a parametric model of the open loop, the fitted model T is then plugged into (1). Of course, it is also possible to apply (1) to the non-parametric estimated frequency response at each frequency, thereby obtaining a nonparametric model of the open loop. Both of those possibilities are compared in Figure 8. They are in close agreement, which is encouraging. Note that while the phase at the first peak of the closed-loop T drops by 180° , indicating a stable pole slightly to the left of the imaginary axis, it increases by 180° in the open-loop response, indicating a pole slightly in the RHP.

Model Validation: Root Locus Analysis

The model F of the open loop obtained in the previous section can now be used to explain the experimental observations. The root locus explains why proportional feedback initially stabilizes the thermoacoustic instability and why a higher-frequency mode becomes unstable at high gains. It will also give a quantitative prediction of that higher frequency, a prediction that can be used to validate the model.

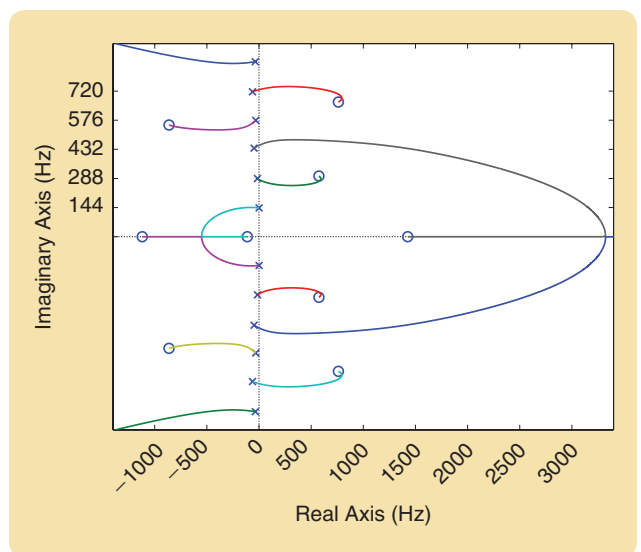


FIGURE 9 A full view of the root locus of the identified open-loop model with variable proportional feedback control gain. The open-loop poles show the (unstable) fundamental mode at 144 Hz and its (stable) harmonics very close to the imaginary axis. Several right-half plane, open-loop zeros attract closed-loop poles into the right-half plane at high feedback control gains.

Figures 8 and 9 show the root locus of the identified open-loop dynamics. The pole pattern resembles that of a damped wave equation, with imaginary parts of the poles being integer multiples of a fundamental frequency and the real parts having successively higher damping as the mode frequency increases. As promised, the fundamental mode is unstable, having a positive real part. The imaginary part of the fundamental mode corresponds to

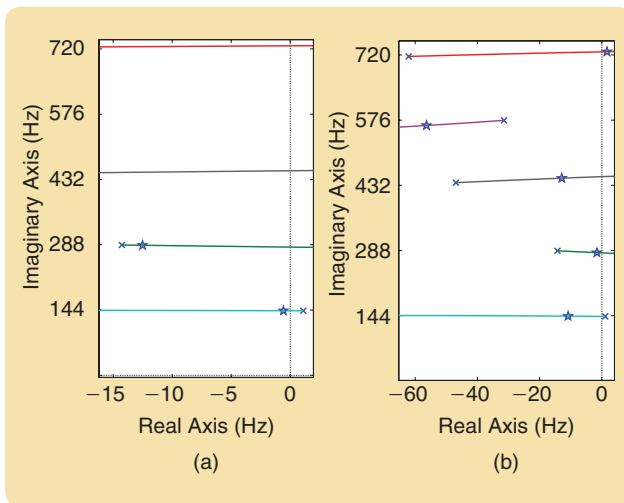


FIGURE 10 Root loci of the identified open-loop model F showing closed-loop pole locations ($*$) at gains that (a) just stabilize the unstable fundamental mode and that (b) make the fifth mode unstable.

the hum frequency heard when the tube is initially powered on.

This system also has multiple RHP zeros that ultimately attract a subset of the initially stable open-loop poles into the RHP, thus causing instability to reoccur at high gains. Figure 10(a) shows the locus and the pole locations at the value of the gain sufficient to initially stabilize the fundamental mode (denoted K_{\min} in Figure 4); all poles are in the left-half plane. However, due to the presence of RHP zeros, some poles will eventually cross into the RHP as the gain is increased. Figure 10(b) indicates that, for this particular

identified model, it is the fifth harmonic mode that becomes unstable at higher gain (denoted K_{\max} in Figure 4). The frequency of this mode must correspond to the frequency of the screech heard in the experiment as the system becomes unstable again at high feedback gains, which is indeed what was observed on the setup used to collect the identification data. This serves as a useful method of model validation.

Common Problems in the Identification Process

Often, the phase of the open-loop frequency response will also drop, instead of increase, by 180° at the first peak, that is, the open loop is identified as stable, while it is known from the initial experiment that the open loop must be unstable. The stability of the open loop is very sensitive to the amplitude and phase of T at the first peak. This is most easily explained with an argument based on the Nyquist criterion. From (1), it is seen that F has the same poles as T in negative unity feedback, so the stability of F can be assessed through the Nyquist criterion. For T to encircle the critical point $(-1,0j)$, requires $|T| > 1$ and $\angle T = -180^\circ$ at the same frequency. Inspecting Figure 6 again, for the presented data, the first peak reaches only about 2 dB, and the range for which it exceeds 0 dB is only about 1 Hz wide. Hence, if the peak is “cut off,” the identification will result in a stable open loop. Likely culprits are insufficient frequency resolution and too much smoothing during the spectral estimation. This situation is detailed in Figure 11. If increasing the resolution and decreasing the smoothing do not help, a different speaker might be the solution; speakers were found to have quite different frequency responses, and some added considerable phase lag.

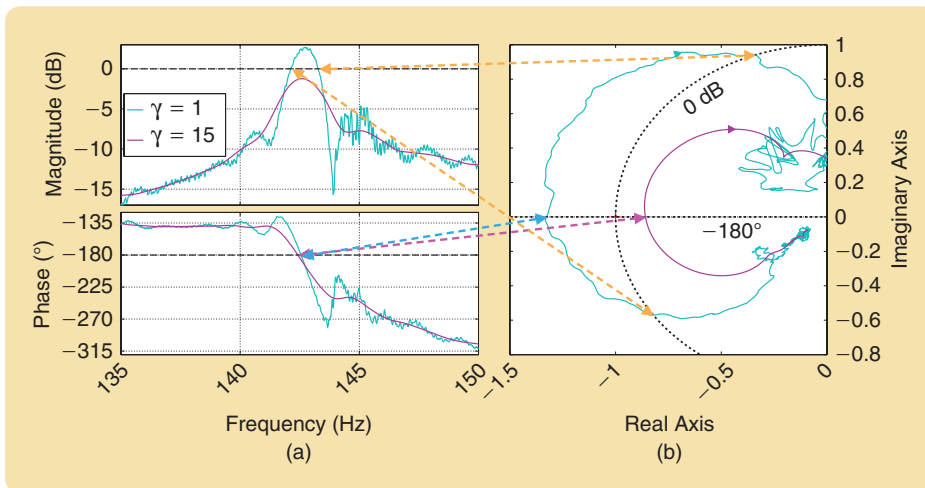


FIGURE 11 By comparing two frequency responses obtained from the same data with different amounts of smoothing (γ is passed to `spafdr` and corresponds roughly to the size of the smallest detail [16]), the difficulty in identifying an unstable open loop can be illustrated. The cyan and magenta frequency responses shown in (a) appear to be qualitatively the same, thus there might be a tendency to choose the magenta one because it looks smoother while still capturing the resonant peak. However, the most important feature—the corresponding unstable open loop—is not captured by this smoother response, which is immediately clear when considering the Nyquist plots shown in (b). The magenta curve cannot loop around the critical point because it never leaves the unit circle. Note that even $\gamma = 15$ still corresponds to relatively little smoothing.

It also might happen that the root locus predicts the higher harmonic instability incorrectly. This again indicates that the initial closed-loop identification step was inaccurately performed (such as insufficient or noisy frequency response data or the order selected for the model fit is too low). A repeat of the identification step with more care will typically resolve this issue, and the more carefully identified model will then yield the correct prediction of the high gain instability.

Finally, if experiments are run for a long time, the tube walls, especially around the heater, absorb a lot of heat. If the identification is stopped and restarted for a new run, there might be no initial

humming, due to the tube walls heating the air around the heater to the point where the heat transfer between air and heater is insufficient to support the humming. In that case, it is necessary to wait for the tube to cool off or, if the setup admits, increase the power to the heater to increase the coil temperature.

Microphone Position

The microphone position generically influences only the location of the zeros, not the poles, which is why its exact position was never stated. However, there are special locations that do yield interesting results. Figure 12 shows the identified open loops if the microphone is placed at three quarters, and at half the length of the tube. Doing so appears to remove peaks. In the former case, it would be every fourth and in the latter case every even-numbered one.

This is relatively easily explained with the physical model of the transfer function developed in the modeling section, but there is also a very intuitive explanation. Each peak corresponds to a mode, that is, a standing pressure wave in the tube. The standing wave corresponding to the first peak is a half-wave, for the second peak a full wave, and so on. Placing the microphone at, for example, the center means placing it where all the even-numbered modes have a pressure node, and hence their contribution is not registered by the microphone, which is a pressure sensor.

This observation would not be surprising for a tube without a heater, but the fact that it still holds true with the heater indicates that the thermoacoustic effect is pulling the first mode into the RHP and that regular acoustics dominate the response.

Estimating the Wire Temperature

Having an estimate of the heating coil's temperature is useful regarding the choice of materials to be used and in the physical modeling process. It is straightforward to obtain a rough estimate from measurements of voltage supplied to, and current drawn by, the heating coil by using the temperature dependence of the electrical resistance of the wire. The resistance R of a wire is commonly assumed to depend on its temperature T affinely

$$R(T) = R_0(1 + \alpha(T - T_0)),$$

where R_0 is the resistance at T_0 , a known point of reference, and α denotes the (linear) temperature coefficient, which is tabulated for different materials. Typically, $\alpha > 0$, that is, the resistance increases as the material heats up; for the Nichrome wire used here, $\alpha \approx 1.76 \cdot 10^{-4}$ 1/K. The relationship can be inverted to give

$$T = T_0 + \frac{R - R_0}{\alpha R_0}.$$

For the reference point (R_0, T_0) , room temperature $T_0 = 293$ K is assumed. The resistance R_0 at room tempera-

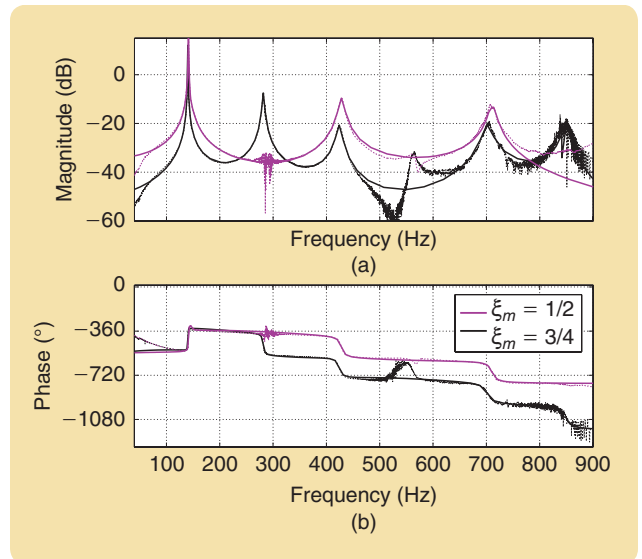


FIGURE 12 Bode plots for identified and fitted open-loop responses with different microphone positions. Placing the microphone in the middle of the tube ($\xi_m = 1/2$) seems to remove every other peak, while placing it at a quarter length from the tube attenuates the fourth peak only. The very ugly identification data at the removed peaks, and especially at the peak around 560 Hz, can be explained by the fact that perfect cancellation of a pole by a zero is virtually impossible. The result is, instead, a pole and a zero very close together, which is notoriously difficult to identify.

ture is estimated by setting the power supply to a small voltage and recording current and voltage across the coil; then the supplied power is increased until the instability sets in, and current and voltage are again recorded. Since current measurements are very noisy, in particular at low voltages, where the signal-to-noise ratio is smaller, averages over relatively long times are taken. An example time trace is shown in Figure 13, resulting in the estimate

$$T_{\text{wire}} \approx 660^\circ\text{C} = 933\text{ K}.$$

It is worth pointing out that while resistive thermometers are based on the same principle, the wire temperature here can by no means be used as a measurement of the gas temperature. For that to be the case, the thermal inertia of the wire would need to be several orders of magnitude smaller, which is why resistive thermometers use extremely thin wires and different materials.

PHYSICAL MODELING OF THE RIJKE TUBE

The remainder of this article is devoted to physical and mathematical modeling of the Rijke tube at several levels of fidelity. The objective is to develop the most parsimonious model from a systems and controls perspective that can explain experimental observations of thermoacoustic instabilities as well as the identification and feedback stabilization results. The key is to model the acoustic dynamics of the tube cavity, which are LTI, and the heat release at the coil, which contains a memoryless

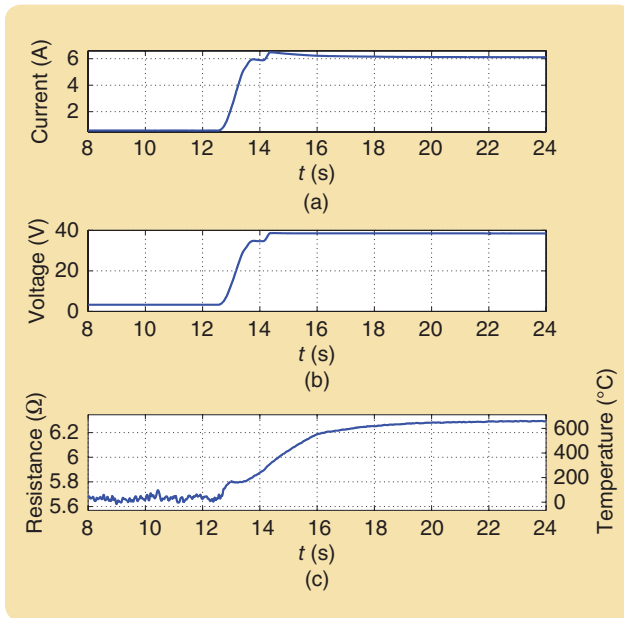


FIGURE 13 Smoothed time traces of voltage and current across the heating coil as the power is first set to a small value and then increased until the humming sets in. Part (c) shows estimated resistance and temperature of the wire.

nonlinearity, separately. The feedback between those two physical phenomena is responsible for the thermoacoustic instability. As in the experimental section, it will

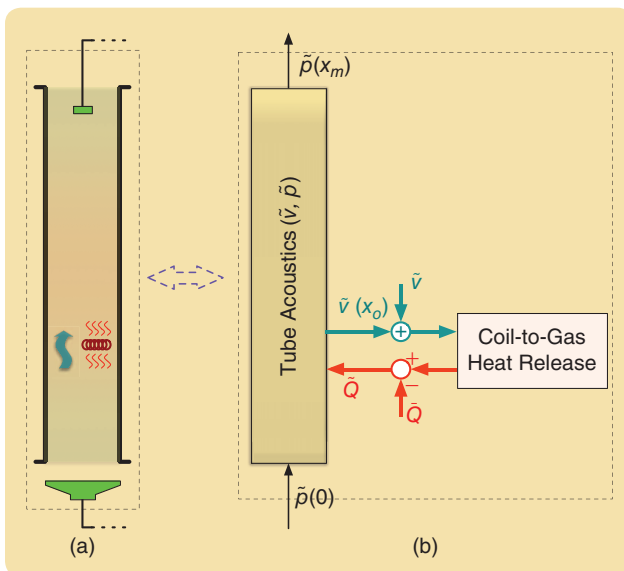


FIGURE 14 A block diagram depiction of the internal and input–output dynamics of the Rijke tube. The “tube acoustics” block models the spatially distributed velocity \tilde{v} and pressure \tilde{p} fluctuations. Speaker and microphone signals are ideally modeled as pressure fluctuations \tilde{p} at the bottom end ($x = 0$) and mic position ($x = x_m$), respectively. The fluctuations \tilde{Q} of heat released from coil to gas act as a source term in acoustic dynamics as depicted by the horizontal arrows in diagram. In turn, this convective heat transfer process is influenced by the absolute gas velocity $\tilde{v} + \tilde{v}(x_0)$ near the coil. This internal feedback coupling between acoustics and heat release dynamics is the cause of the thermoacoustic instability.

be seen that LTI systems tools can explain much of the above phenomena.

A summary of the modeling results and their predictions about the instability is given next. This summary section can be largely read on its own; it assumes certain models for acoustics and heat transfer that are interpreted and motivated physically. Detailed derivations are postponed to subsequent sections for those readers interested in delving deeper.

Summary of Modeling and Analysis Results

A control-oriented model and physical description of the basic thermoacoustic dynamics can be summarized using two descriptive diagrams. Begin with Figure 14, where “tube acoustics” represents the dynamics of the velocity and pressure fluctuations \tilde{v} and \tilde{p} . These are the fluctuations of the actual flow velocity v and pressure p about the nominal values \bar{v} (the steady upward velocity) and \bar{p} (atmospheric pressure), respectively. These fluctuations are also referred to as “acoustic velocity” and “acoustic pressure.” Both velocity and pressure fluctuations are fields that vary along the length of the tube, while the nominal \bar{v} and \bar{p} are assumed to be constant in both time and space. As demonstrated later, the dynamics of (\tilde{v}, \tilde{p}) are described by a one-dimensional wave equation with the speaker (actuator) input modeled as a pressure boundary condition, while the microphone signal is the value of the pressure field at the microphone location. These acoustic dynamics constitute an LTI (though infinite-dimensional) system.

The second ingredient is to model the interaction between the heater coil and the surrounding air. In a steady situation with constant upward flow, heat is transferred from the heater to the upward-flowing gas conductively as well as convectively. The *convective* heat transfer is a function of flow velocity: the higher the velocity, the more heat is transferred from the coil to the gas. If flow velocity near the heater is fluctuating (in time), then the amount of heat transferred from coil to gas also fluctuates in response. This is shown in Figure 14 as a green wavy arrow depicting velocity fluctuations and red waves depicting fluctuations of heat released from the coil. The block labeled “coil-to-gas heat release” represents the effect of local velocity fluctuations $\tilde{v}(t, x_0)$ on fluctuations $\tilde{Q}(t)$ in the amount of heat released. On the other hand, as will be demonstrated later, $\tilde{Q}(t)$ acts as a source term in the gas dynamics (10) and can therefore be considered as an input to the acoustic part of the model. Within the “tube acoustics” block, there is an acoustic feedback path from $\tilde{Q}(t)$ back to $\tilde{v}(t, x_0)$ that, as explained earlier, drives $\tilde{Q}(t)$ through the heat release mechanism.

Figure 15 describes this feedback mechanism in a little more detail. The center block G is the LTI 2×2 transfer function matrix of the acoustics from the inputs to the outputs, as depicted in Figure 14. This matrix is made up of transcendental transfer functions, since the underlying dynamics are infinite dimensional. For example, with

undamped acoustics, coil location $x_o = L/4$, and microphone position $x_m > L/4$, the matrix is

$$G(s) = \begin{bmatrix} \frac{\sinh\left(\frac{(L-x_m)s}{c}\right)}{\sinh\left(\frac{Ls}{c}\right)} & \frac{\bar{\gamma}}{c} \frac{\sinh\left(\frac{L}{4c}s\right)\sinh\left(\frac{(L-x_m)s}{c}\right)}{\sinh\left(\frac{Ls}{c}\right)} \\ \frac{1}{\bar{\rho}c} \frac{\cosh\left(\frac{3L}{4c}s\right)}{\sinh\left(\frac{Ls}{c}\right)} & -\frac{\bar{\gamma}}{4\bar{\rho}c^2} \frac{1}{\cosh\left(\frac{Ls}{2c}\right)} \end{bmatrix}; \quad (3)$$

for values and explanations of the involved parameters, see Table 1. $G(s)$ is derived in the remaining sections, in particular “Transfer Function Computation for Two-Point Boundary Value Problems.”

The transfer function $G_{22}(s)$ is important for understanding the thermoacoustic instability since it is in feedback with the heat release dynamics. Note that on the imaginary axis

$$\cosh\left(\frac{L}{2c}j\omega\right) = \cos\left(\frac{L}{2c}\omega\right),$$

and therefore G_{22} has infinitely many poles on the imaginary axis at

$$\omega_k = (2n-1)\frac{c\pi}{L}, \quad n \in \mathbb{Z},$$

that correspond to the odd acoustic modes of a tube with two open ends, that is, standing waves with wavelengths of $2L, 2L/3, 2L/5$, and so on. The fundamental mode corresponds to $n = 1$ and is the one depicted in Figure 3. If damping and/or radiative effects were to be included, those poles would be shifted to the left in a similar manner to those in Figure 9; this issue is further elaborated in “Wave Dynamics with Diffusion and Damping.” The important fact to keep in mind is that G_{22} has *many very lightly damped poles* arranged at integer multiples of a fundamental frequency.

The heat release dynamics in the bottom blocks of Figure 15 combine two effects, with the simpler one being a first-order lag with time constant t_{hr} representing the “thermal inertia” of the boundary layer surrounding the coil. The second effect is the square-root dependence of heat release on velocity. This is known as King’s law [20], and it reflects that convective heat transfer is enhanced by increasing velocity, but the “enhancement rate” decreases as velocity increases. This effect of diminishing returns of heat release is responsible for the fact that an instability in the feedback loop between G_{22} and heat release ultimately produces a stable limit cycle. This is similar to what occurs in linearly unstable loops containing a saturation-type memoryless nonlinearity. The exponentially growing response due to the instability ultimately saturates, producing a stable limit cycle.

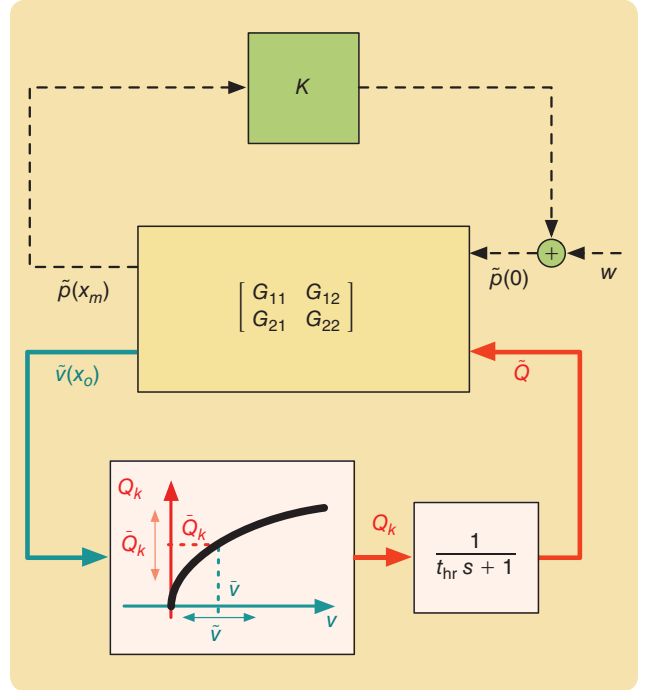


FIGURE 15 The nature of the feedback between acoustics and heat release depicted in Figure 14. The linear time-invariant acoustic dynamics transfer functions $G_{ij}(s)$ have lightly damped modes, which are in feedback with a first-order lag and a memoryless square-root-type nonlinearity characterizing convective heat release. As a mapping from \tilde{v} to \tilde{Q} , the nonlinearity can appear as either high or low feedback gain at small or large amplitudes of \tilde{v} , respectively. At small \tilde{v} amplitudes, the lightly damped modes of the acoustics are destabilized by the high “effective gain” of heat release. As amplitudes of \tilde{v} increase, the effective feedback gain decreases so that conditions for a stable limit cycle are achieved.

Hence, the heat release dynamics constitute a feedback from acoustic velocity to heat transfer. It is very important to distinguish this feedback from the stabilizing proportional feedback of the preceding section. On the one hand, the heat release process can be *interpreted as an internal* feedback loop because it connects two signals not accessible to measurement or direct manipulation. On the other hand, the stabilizing feedback is an *external* controller. Thus, the *open* loop identified in the previous section corresponds to the transfer function from $\tilde{p}(0)$ to $\tilde{p}(x_m)$ in Figure 15, which includes the *closed* loop of G_{22} and heat release. The above qualitative arguments hint that the key to quantitative understanding of the thermoacoustic instability is analyzing the linearization of this internal feedback loop, consisting of G_{22} , the first-order lag, and the linearization of the heat release square-root law, which can be modeled as a variable linear gain. It turns out that a root locus analysis accurately describes the effect of this gain, as is demonstrated next.

The open-loop transfer function of the linearization of the lower feedback loop in Figure 15 is

$$-\frac{\bar{\gamma}}{4\bar{\rho}c^2} \frac{1}{\cosh\left(\frac{L}{2c}s\right)} \frac{1}{t_{hr}s + 1} f'(\tilde{v}),$$

Transfer Function Computation for Two-Point Boundary Value Problems

A unified way to treat linear two-point boundary value problems can be described by using the first-order form, which is a state-space realization with space x as the independent variable

$$\frac{d}{dx} \psi(x) = F\psi(x) + G\delta(x - x_o)r, \quad x \in [x_i, x_f], \quad (S2)$$

$$N_u u = N_i \psi(x_i) + N_f \psi(x_f). \quad (S3)$$

The first equation is the differential equation, while the second expresses general linear boundary conditions. The inputs r and u can be regarded as parameters. The objective is to obtain a formula for the solution $\psi(x)$ as a function of r and u . The matrices F and G may depend on other parameters (for example, the Laplace transform variable s), and the formula obtained applies to such cases as well.

The presence of $\delta(x - x_o)$ in the r input term implies that the solution $\psi(x)$ could have a discontinuity at x_o but is continuous everywhere else. As shown in Figure S2, the upper and lower limits at the jump point x_o ,

$$\psi(x_o^+) := \lim_{x \searrow x_o} \psi(x), \quad \psi(x_o^-) := \lim_{x \nearrow x_o} \psi(x),$$

satisfy the relation [which follows from (S2)]

$$\psi(x_o^+) = \psi(x_o^-) + G r. \quad (S4)$$

The solution over each of the intervals $[x_i, x_o]$ and $[x_o, x_f]$ can be propagated from each end

$$\psi(x) = \begin{cases} \Phi(x, x_i) \psi(x_i), & x \in [x_i, x_o] \\ \Phi(x, x_f) \psi(x_f), & x \in [x_o, x_f] \end{cases} \quad (S5)$$

where $\Phi(x_1, x_2) = e^{F(x_1 - x_2)}$ for the constant coefficient ODE (S2). The jump relation (S4) can now be rewritten by first observing that (S5) gives

$$\begin{aligned} \psi(x_o^-) &= \Phi(x_o, x_i) \psi(x_i), \\ \psi(x_i) &= \Phi(x_i, x_o) \psi(x_o^+), \end{aligned}$$

which, combined with (S4), yields a relation between $\psi(x_i)$ and $\psi(x_f)$ as a function of the input r

$$\psi(x_f) = \Phi(x_f, x_o) (\Phi(x_o, x_i) \psi(x_i) + G r). \quad (S6)$$

The given boundary conditions (S3) can now be combined together with (S6) in the following matrix-vector form

$$\begin{bmatrix} -\Phi(x_f, x_i) & 1 \\ N_i & N_f \end{bmatrix} \begin{bmatrix} \psi(x_i) \\ \psi(x_f) \end{bmatrix} = \begin{bmatrix} \Phi(x_f, x_o)G & 0 \\ 0 & N_u \end{bmatrix} \begin{bmatrix} r \\ u \end{bmatrix}.$$

Finally, this permits rewriting the solution (S5) in terms of the inputs r and u as

$$\psi(x) = \begin{cases} [\Phi(x, x_i) \ 0] \Gamma \begin{bmatrix} r \\ u \end{bmatrix}, & x \in [x_i, x_o], \\ [0 \ \Phi(x, x_f)] \Gamma \begin{bmatrix} r \\ u \end{bmatrix}, & x \in [x_o, x_f], \end{cases}$$

where

$$\Gamma = \begin{bmatrix} -\Phi(x_f, x_i) & I \\ N_i & N_f \end{bmatrix}^{-1} \begin{bmatrix} \Phi(x_f, x_o)G & 0 \\ 0 & N_u \end{bmatrix}.$$

Depending on the system structure, the value of ψ at x_o might be discontinuous. The average value at the point x_o is written as

$$\psi_{av}(x_o) = \frac{1}{2} [\Phi(x_o, x_i) \ \Phi(x_o, x_f)] \Gamma \begin{bmatrix} r \\ u \end{bmatrix}. \quad (S7)$$

Note that the basic computation is that of $\Phi(\cdot, \cdot)$, which can be done analytically with computer algebra routines for systems of order four or lower. This corresponds to PDEs in which the spatial derivative order is four or lower, which is the case for the wave equation studied in this article.

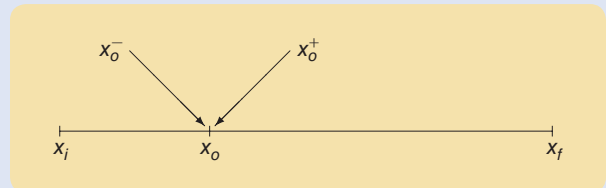


FIGURE S2 An illustration of the jump point at x_o .

where $f'(\bar{v})$ is the derivative of the square-root nonlinear gain at the steady upward flow velocity \bar{v} ; see also (8) and (14). This represents a linear positive feedback gain that depends on the operating condition \bar{v} . Thus, the stability of the linearized closed-loop system can be completely characterized using the (negative gain) root locus of the transfer function

$$L(s) = \frac{1}{\cosh\left(\frac{L}{2c}s\right)} \frac{1}{t_{hr}s + 1}. \quad (4)$$

Since this transfer function has infinitely many poles, a little care is needed in generating the root locus. Figure 16 shows the locus of the zeros of $1 + kL(s)$ using a continuation (Newton) method in the positive real parameter k . The open-

loop poles are the acoustic ones lying on the imaginary axis together with one pole on the negative real axis corresponding to the first-order lag in heat release dynamics. In reality, the acoustics have some damping and the corresponding poles lie slightly to the left of the imaginary axis, as for example in Figure 9. Therefore, the open-loop dynamics are stable but have an array of very lightly damped poles. With the positive feedback from coil heat release, half of the acoustic poles eventually move into the RHP. The first pole (pair) to cross into the RHP corresponds to the fundamental frequency and is depicted by the red branches in Figure 16. Its imaginary-axis-crossing frequency of 141 Hz corresponds almost exactly to the frequency of the hum recorded at the onset of thermoacoustic instability. Once this instability is triggered,

Wave Dynamics with Diffusion and Damping

Adding thermal diffusion, viscosity, and wall friction to the equations in the right-hand column of Table S1, linearizing, and rewriting in nondimensional form as outlined in “Dimensionless Quantities,” gives

$$\begin{aligned} \frac{\partial}{\partial \tau} \begin{bmatrix} \tilde{r} \\ \tilde{m} \\ \tilde{\psi} \end{bmatrix} &= \begin{bmatrix} 0 & 0 & 0 \\ \text{Ma}\bar{\beta} & -\bar{\beta} & 0 \\ 0 & 2\text{Ma}\gamma\bar{\beta} & 0 \end{bmatrix} \begin{bmatrix} \tilde{r} \\ \tilde{m} \\ \tilde{\psi} \end{bmatrix} - \begin{bmatrix} \text{Ma} & 1 & 0 \\ 0 & \text{Ma} & \frac{1}{\gamma} \\ 0 & \gamma & \text{Ma} \end{bmatrix} \frac{\partial}{\partial \xi} \begin{bmatrix} \tilde{r} \\ \tilde{m} \\ \tilde{\psi} \end{bmatrix} \\ &+ \phi \begin{bmatrix} 0 & 0 & 0 \\ 0 & \text{Pr}/\gamma & 0 \\ -1 & 0 & 1 \end{bmatrix} \frac{\partial^2}{\partial \xi^2} \begin{bmatrix} \tilde{r} \\ \tilde{m} \\ \tilde{\psi} \end{bmatrix} + \begin{bmatrix} 0 \\ 0 \\ \dot{q} \end{bmatrix}, \end{aligned} \quad (\text{S8})$$

where $\text{Pr} = \nu/\alpha$ is the Prandtl number, the ratio of kinematic viscosity and thermal diffusivity, ϕ is a dimensionless diffusion strength parameter, and $\bar{\beta}$ quantifies the amount of friction; for details on the derivation, see [34].

The complexity of the model has increased significantly: (S8) is of second order, due to diffusion, and in three states, since the density \tilde{r} is not decoupled anymore. In principle, the procedure of “Transfer Function Computation for Two-Point Boundary Value Problems” can still be applied, but the obtained transfer functions are too unwieldy to learn anything from them. However, the poles of any derived transfer function will be a subset of the spectrum of the right-hand-side operator, analogously to the situation in finite-dimensional LTI systems. Hence, instead of transfer function computations, the spectrum of the right-hand-side operator is computed numerically using Chebyshev spectral methods. For details on and more applications of such methods, refer to the excellent book [35].

Figure S3 shows the significant part of the spectrum obtained using $N = 192$ grid points, along with some of the pressure modes for a specific set of the parameters Ma , Pr , ϕ , and $\bar{\beta}$ representative of the conditions in the Rijke tube experiment. As expected, the spectrum is located very close to, but to the left of, the imaginary axis, with modes corresponding to a standing half-wave and its harmonics; poles corresponding to higher frequencies are farther left, indicating more damping. It is important to note that, in particular, the parameters ϕ and $\bar{\beta}$, which are known only to within maybe an order of magnitude, appear to have very well-

defined effects. Increasing the amount of diffusion ϕ will bend the spectrum, that is, the parabola shape will become narrower, while increasing the amount of friction $\bar{\beta}$ will shift the entire spectrum toward the left. These numerical computations validate the claim made during the analysis of the root locus in Figure 16, namely that the poles located on the imaginary axis would be shifted toward the left if neglected diffusion and/or damping effects were retained.

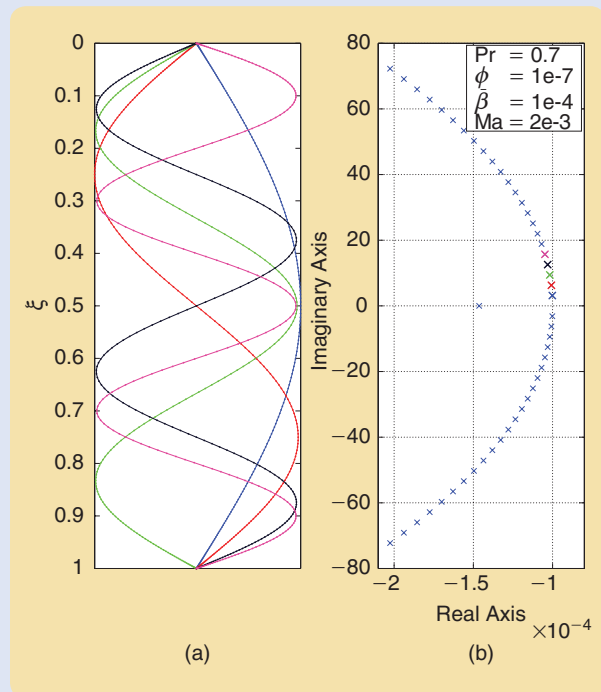


FIGURE S3 A numerical computation of the spectrum of the spatial differential operator in (S8). Part (a) shows the five pressure modes corresponding to the fundamental and the first four harmonics; they are indistinguishable from the pressure modes of the undamped model (11), corresponding to the resonances of a tube with two open ends. Part (b) shows part of the numerically computed spectrum. Poles located on the imaginary axis in the case without damping are now damped, that is, shifted to the left. Higher frequencies are damped more but still lightly damped (note the axis scales).

the system exhibits growing oscillations and leaves the linear regime (remember, the $\tilde{\tau}$ variables need to be small). Intuitively, the square-root term then offers diminishing returns, that is, at higher acoustic velocities, it almost saturates, and even larger oscillations in velocity are not supported by the enhanced heat transfer. The system is brought into a limit cycle, the shape of which can be seen in Figure 2(c).

While in the literature, the Rijke tube is typically modeled as consisting of two or three compartments—a cold zone below the heater, a hot zone above it, and sometimes a small zone in which the heat exchange takes place—and the heater is introduced as causing a discontinuity in the velocity field [9], the tube is modeled in one piece in the following

derivation. This approach avoids explicit introduction of time delays to account for sound waves traveling through cold and hot zones [13], [21], [22]. The hyperbolic functions can be interpreted in (3) to contain delays but, as will be seen, they result naturally from the spatially distributed modeling process; see also “One-Dimensional Compressible Gas Dynamics” and “Transfer Function Computation for Two-Point Boundary Value Problems.”

Acoustic Dynamics from Mass, Momentum, and Energy Balances

The basic features of the Rijke tube experiment can be captured using a simplified model of one-dimensional

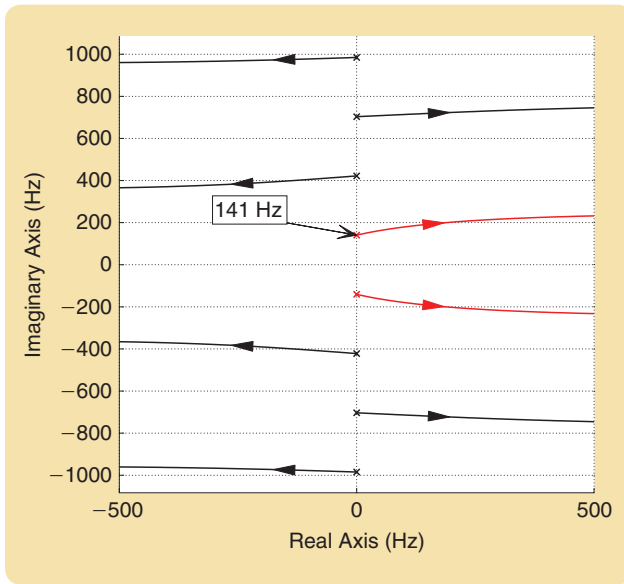


FIGURE 16 The root locus for the feedback interconnection of $G_{22}(s)$ and the linearized heat release dynamics in Figure 15. The plot should be interpreted as if it were shifted slightly to the left, as would be the case if realistic damping effects were included. The branch shown in red corresponds to the thermoacoustic instability. Assuming standard conditions on air, its crossover point is at 141 Hz, very close to the frequency of the observed hum and the 144 Hz predicted by the identified model; see Figure 10. See Table 1 for the parameter values used.

compressible gas dynamics. A brief description and derivation of the Euler equations of gas dynamics in one dimension is included in “One-Dimensional Compressible Gas Dynamics.” These are partial differential equations (PDEs) that describe conservation of mass, momentum, and energy, respectively. They can be written in several forms, and the form chosen here is the one that relates the time-varying density $\rho(t,x)$, velocity $v(t,x)$, and pressure $p(t,x)$ distributions along the axial dimension x of the tube. The one-dimensional model is a reasonable approximation to the true three-dimensional physics since the Rijke tube has a high aspect ratio, and therefore the important fluctuations of ρ , v , and p are primarily in the axial direction. The equations are

$$\begin{bmatrix} \frac{\partial \rho}{\partial t} \\ \frac{\partial v}{\partial t} \\ \frac{\partial p}{\partial t} \end{bmatrix} = - \begin{bmatrix} v & \rho & 0 \\ 0 & v & \frac{1}{\rho} \\ 0 & \gamma p & v \end{bmatrix} \begin{bmatrix} \frac{\partial \rho}{\partial x} \\ \frac{\partial v}{\partial x} \\ \frac{\partial p}{\partial x} \end{bmatrix} + \begin{bmatrix} 0 \\ 0 \\ \tilde{\gamma} q \end{bmatrix}, \quad (5)$$

where $q(t,x)$ denotes the external heat power added per unit volume and acts as an input (source term). The nonlinear equations are written in a matrix-vector form that is convenient later for linearization. Depending on the steady conditions about which these equations are linearized, the resulting linearization is a one-dimensional linear PDE that looks like a wave equation and thus describes acoustic wave propagation. The linearization of the above equations will form the “tube acoustics” block in Figures 13 and 14.

Actuation and Sensing

The Rijke tube has both ends open, which is typically modeled by having pressure boundary conditions held at the ambient atmospheric pressure. The bottom end, however, is very close to the actuating speaker, and while a true model of the influence of the speaker involves accounting for inward radiating waves, a simple and reasonable approximation is to assume the speaker signal causes pressure fluctuations at the bottom end. Thus, the pressure boundary conditions for the system (5) are

$$\begin{aligned} p(t,0) &= p_0 + u(t), \\ p(t,L) &= p_0, \end{aligned} \quad (6)$$

where p_0 is the ambient pressure, and $u(t)$ is the speaker signal. A correction term could be introduced into the boundary conditions to account for the fact that, in reality, the nodes lie slightly outside the tube [10]. Since the effect of the end correction is small, an additional complication is avoided by neglecting this.

Note that $u(t)$ acts as an input to the gas dynamics, but it is not distributed. The same holds for the measurement through a microphone, which is a pressure sensor whose output is (proportional to) the pressure $p(t,x_m)$ at the microphone location x_m . The controller used to stabilize the tube connects those two signals via a proportional control feedback loop.

Heat Transfer

The Euler equations (5) have an external heat input $q(t,x)$ as a source term, which can be used to model heat released from the coil into the gas. If the coil is assumed to be located in a very narrow section at location x_o , then a reasonable approximation to this distributed input is

$$q(t,x) = \frac{1}{A} \delta(x - x_o) Q(t), \quad (7)$$

where δ is the Dirac impulse with units 1/m, $Q(t)$ is the heat power released from the coil in W, and A is the tube cross section.

The next key step is to quantify the dependence of coil-to-gas heat power released $Q(t)$ on the flow velocity $v(x_o,t)$ near the wire. Heat is transferred from a solid to a gas due to both conduction and convection. Convection depends on the velocity v of the gas, whereas conduction does not; both depend on the temperature difference. King’s law [20] is a commonly used approximation for these dependencies, and in the current context it states that in steady flow, the heat power transfer Q_K of a hot circular wire of length l_w in a colder fluid flow is

$$Q_K = l_w (\kappa + \kappa_v \sqrt{|v|}) (T_{\text{wire}} - T_{\text{gas}}), \quad (8)$$

where κ is the fluid’s thermal conductivity, and κ_v is a constant that is largely empirically determined. The first term is Fourier’s law of heat conduction, while the second term

One-Dimensional Compressible Gas Dynamics

Acoustic phenomena occur in compressible fluids. In full generality, the dynamics of such fluids are often modeled by the Euler equations of gas dynamics. Since the Rijke tube has a high aspect ratio, the geometry is simplified so that all variations of pressure, density, and velocity can be assumed to occur only along the axial direction. Therefore, a simpler one-dimensional mathematical model of compressible gas dynamics is sufficient to describe thermoacoustic phenomena in the Rijke tube. The three physical laws of 1) conservation of mass, 2) momentum balance, and 3) energy balance can be used to derive three PDEs for one-dimensional gas dynamics as shown here. To begin with, consider a one-dimensional medium with a control volume between x_1 and x_2 as illustrated in Figure S4. Let $\psi(t, x)$ and $\phi(t, x)$ be two spatially distributed fields that satisfy a flux-type relationship

$$\frac{d}{dt} \left(\int_{x_1}^{x_2} \psi(t, x) dx \right) = \phi(t, x) \Big|_{x_1}^{x_2},$$

which states that the time rate of change of the total quantity of ψ in $[x_1, x_2]$ is given by the value of ϕ at the boundaries x_1 and x_2 . Dividing the above equation by $(x_2 - x_1)$ and taking the small-volume limit of $(x_2 - x_1) \rightarrow 0$ results in the PDE

$$\frac{\partial \psi}{\partial t}(t, x) = \frac{\partial \phi}{\partial x}(t, x).$$

This accounting procedure can now be performed for the gas density $\rho(t, x)$, momentum $\rho(t, x)v(t, x)$, and internal energy $\rho(t, x)U(t, x)$ distributions. For a calorically perfect gas that also satisfies the ideal gas law, the internal energy (which accounts for the energy stored in molecular motion and vibration) can be expressed in terms of the pressure field by $\rho(t, x)U(t, x) = (c_v/R)\rho(t, x)$, where c_v and R are the specific heat capacity and universal gas constant, respectively. The deri-

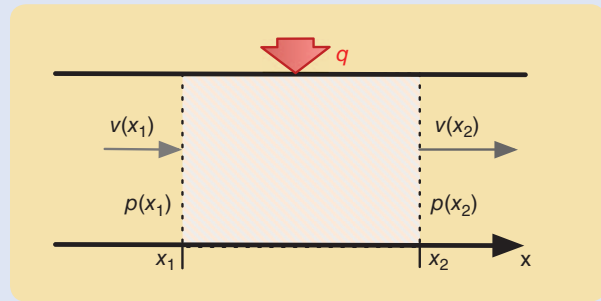


FIGURE S4 A small control volume used to account for density, momentum, and energy balances in a one-dimensional model. The time rate of change of a quantity inside the volume $[x_1, x_2]$ is equal to the flux through the boundaries x_1 and x_2 of quantities that influence it.

vation of the three physical laws is outlined in Table S1 in a simplified setting that neglects effects such as heat conduction within the gas, its viscosity, and external forces. These effects can be easily added to that derivation as needed.

An exercise in algebra and the product rule of differentiation allows rewriting the PDEs of Table S1 in the following more standard form

$$\frac{\partial}{\partial t} \begin{bmatrix} \rho \\ v \\ p \end{bmatrix} = - \begin{bmatrix} v & \rho & 0 \\ 0 & v & 1 \\ 0 & \gamma p & v \end{bmatrix} \begin{bmatrix} \frac{\partial \rho}{\partial x} \\ \frac{\partial v}{\partial x} \\ \frac{\partial p}{\partial x} \end{bmatrix} + \begin{bmatrix} 0 \\ 0 \\ \gamma q \end{bmatrix},$$

where $\gamma = 1 + R/c_v$ is the heat capacity ratio of the gas ($\gamma = 1.4$ for diatomic gases like air), $\bar{\gamma} = \gamma - 1$, and $q(t, x)$ denotes the heat power added per unit volume. These equations are the one-dimensional version of the Euler equations of gas dynamics; the matrix-vector form they are written in is particularly convenient for linearization.

TABLE S1 A derivation of the basic partial differential equations of one-dimensional gas dynamics.

Balance in Control Volume

Mass conservation

$$\frac{d}{dt} \underbrace{\int_{x_1}^{x_2} \rho dx}_{\text{total mass in control volume}} = \underbrace{-\rho v \Big|_{x_1}^{x_2}}_{\text{total inflow through boundaries}}$$

Momentum balance

$$\frac{d}{dt} \underbrace{\int_{x_1}^{x_2} \rho v dx}_{\text{total momentum in control volume}} = \underbrace{-v(\rho v) \Big|_{x_1}^{x_2}}_{\text{momentum inflow through boundaries}} - \underbrace{p \Big|_{x_1}^{x_2}}_{\text{total force at boundaries}}$$

Energy balance

$$\frac{d}{dt} \underbrace{\int_{x_1}^{x_2} \left(\rho U + \frac{\rho v^2}{2} \right) dx}_{\text{total energy in control volume}} = \underbrace{-v \left(\rho U + \frac{\rho v^2}{2} \right) \Big|_{x_1}^{x_2}}_{\text{Power added by material inflow}} - \underbrace{p v \Big|_{x_1}^{x_2}}_{\text{work rate of pressure forces}} + \underbrace{\int_{x_1}^{x_2} q dx}_{\text{heat power added}}$$

PDE

$$\frac{\partial}{\partial t} \rho + \frac{\partial}{\partial x} (\rho v) = 0$$

$$\frac{\partial}{\partial t} (\rho v) + \frac{\partial}{\partial x} (\rho v^2 + p) = 0$$

$$\frac{\partial}{\partial t} \left(\rho U + \frac{\rho v^2}{2} \right) + \frac{\partial}{\partial x} \left(v \left(\rho U + \frac{\rho v^2}{2} \right) + p v \right) = q$$

expresses that convective heat transfer occurs at a rate proportional to $\sqrt{|v|}$. The formula suggests that heat transfer is enhanced by flow velocity, regardless of direction, but the “rate of enhancement” tapers off as velocity increases.

King’s law does not include any temporal dynamics. However, if the gas velocity fluctuates, there are important dynamic effects to be considered, and it will turn out that their inclusion is crucial to correctly predicting the frequency of the hum. These dynamics are mainly due to a boundary layer forming around the wire, which has its own thermal inertia. Figure S3 and “Boundary-Layer Effect on Heat Release” explain this effect. An intuitive picture is to imagine this boundary layer as a blob of stagnant air, through which the heat needs to be conducted before reaching the free stream of gas outside the boundary layer. The conclusion is that this boundary-layer effect introduces a first-order lag into the heat release process, which now can be modeled by

$$t_{hr} \dot{Q}(t) = -Q(t) + Q_K(t), \quad (9a)$$

$$Q_K(t) = I_w(T_{wire} - T_{gas}) (\kappa + \kappa_v \sqrt{|v(t, x_0)|}). \quad (9b)$$

Note how the mapping from $v(\cdot, x_0)$ to Q_K in (9b) is the memoryless nonlinearity in the bottom loop of Figure 15, while (9a) represents the first-order lag.

Equation (9) tacitly assumed that T_{gas} is constant, but in reality it fluctuates together with pressure and density. It is shown in a subsequent section (see Figure 17) that this effect is much less significant than the dependence on velocity fluctuations, and therefore Figure 15 has only the velocity fluctuations as an input to the heat release mechanism.

Linearization of the Acoustics

The full system is described by the gas dynamics (5), the boundary conditions (6), and heat input (7), which are in

Boundary-Layer Effect on Heat Release

When heat is transferred from a hot surface to a gas in steady relative motion, the heat transfer coefficient’s dependence on gas velocity is captured by King’s law

$$\text{heat transfer coefficient} \sim \kappa + \kappa_v \sqrt{|v|}. \quad (S9)$$

When gas velocity is not constant but fluctuating, this dependence has dynamics as well, as discussed in Figure S5. Lighthill [33] analyzed these dynamics in great detail; incidentally, the author was inspired to conduct this investigation by the Rijke tube. Whenever flowing fluid comes into contact with a solid, a boundary layer is formed, and it is found that the thermal inertia of

the boundary layer around the wire can be modeled by a simple first-order lag, that is, a transfer function of the form $1/(t_{hr}s + 1)$. An estimate for the corresponding time constant is given by [33]

$$t_{hr} = 0.2 \frac{d_{wire}}{\bar{v}} = \frac{\text{diameter of the wire}}{5 \cdot \text{steady free-stream velocity}}.$$

Cascading the static and dynamic dependence of the heat transfer on the velocity leads to the model (9).

As has been observed in [33] already, this lag, even if it is very small, is crucial for the model to be valid. In the current setting, this can be demonstrated nicely by considering the root locus for the model without lag (corresponding to $t_{hr} \equiv 0$), shown in Figure S6. This root locus predicts a humming frequency of roughly 282 Hz, which is twice what is observed in experiments.

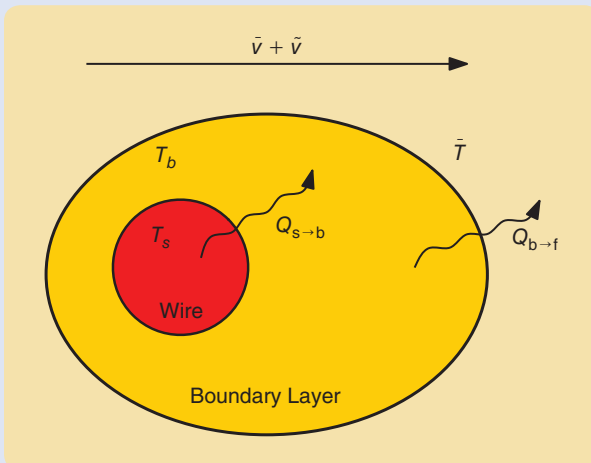


FIGURE S5 An illustration of the boundary layer’s effect on coil-to-gas heat transfer. Intuitively, the boundary layer depicted by the orange ellipse can be imagined as a blob of stagnant air. Heat transfer from the boundary layer into the free stream, denoted by $Q_{b \rightarrow f}$, reacts instantly to changes in the free stream velocity $\bar{v} + \tilde{v}$ according to King’s law (S9), but heat $Q_{s \rightarrow b}$ transferred from the wire needs to propagate through the boundary layer before reaching the free stream, leading to a first-order lag from flow velocity \tilde{v} to heat release \tilde{q} fluctuations.

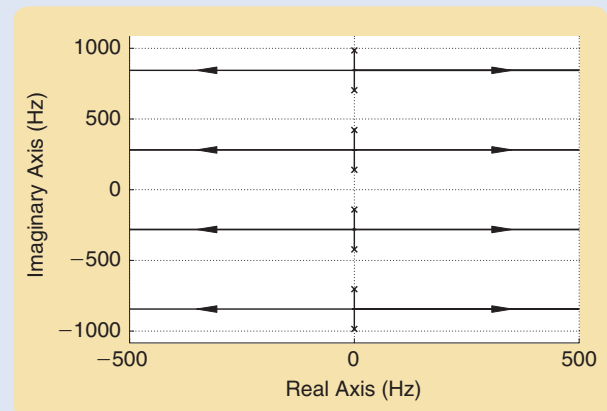


FIGURE S6 What the root locus of Figure 16 would look like if the wire’s thermal boundary-layer effect was ignored. This amounts to assuming $t_{hr} = 0$ or equivalently ignoring the first-order lag in the heat-release response. The fundamental frequency branch that moves into the right-half plane is now incorrectly predicted to be twice what is observed in experiments. This illustrates that including the first-order lag is crucial to correctly predict thermoacoustic instabilities.

feedback with the heat release model consisting of King's law (9b) and the first-order lag (9a) of the boundary-layer effect. The two subsystems of gas dynamics and heat release can be linearized separately. The linearization of the former yields linear acoustic dynamics, and while the linearization of the latter is straightforward, an analysis of the involved parameters reveals that velocity fluctuations are significantly more important than pressure and density fluctuations in the feedback path.

Linearization of the nonlinear model (5) requires knowing the steady-state conditions. An accurate calculation of the steady state requires incorporating buoyancy effects (to model steady upward flow due to steady heat release from the coil) as well as the steady temperature and density variations along the tube length (for example, gas in the upper section is hotter than that in lower section). However, since the important parameter in acoustic dynamics is the speed of sound, and the above variations have relatively minor effect on the speed of sound, an alternative and much simpler equilibrium can be used for the acoustic linearization. This simple equilibrium assumes spatially constant density, velocity, and pressure fields, which trivially satisfy the nonlinear PDEs, if there is no heat input ($q \equiv 0$) and no speaker actuation ($u \equiv 0$). Denoting a steady state by a bar $\bar{\cdot}$ and small deviations from it by a tilde $\tilde{\cdot}$, a linearization is obtained by plugging $\rho(t,x) = \bar{\rho} + \tilde{\rho}(t,x)$ and so on into the nonlinear equations and discarding all terms of second or higher order in the deviation variables. Applying this process to (5) leads to

$$\frac{\partial}{\partial t} \begin{bmatrix} \tilde{\rho} \\ \tilde{v} \\ \tilde{p} \end{bmatrix} = - \begin{bmatrix} \tilde{v} & \tilde{\rho} & 0 \\ 0 & \tilde{v} & \frac{1}{\tilde{\rho}} \\ 0 & \gamma \tilde{p} & \tilde{v} \end{bmatrix} \frac{\partial}{\partial x} \begin{bmatrix} \tilde{\rho} \\ \tilde{v} \\ \tilde{p} \end{bmatrix} + \begin{bmatrix} 0 \\ 0 \\ \tilde{\gamma} \end{bmatrix} \tilde{q}, \quad (10)$$

which very closely resembles (5) with the important difference that the "A-matrix" is now a constant matrix and hence, (10) is a linear, but infinite-dimensional, state-space description of the gas dynamics with the state $[\tilde{\rho} \ \tilde{v} \ \tilde{p}]^T$. Furthermore, from (6) it follows immediately that $\tilde{p} = p_0$, and that $\tilde{p}(t,0) = u(t)$ and $\tilde{p}(t,L) = 0$.

A further simplification is due to the upward flow \bar{v} being very small (relative to the speed of sound). Rewriting the model in dimensionless quantities shows that if $\bar{v} \ll c$, where $c = \sqrt{\gamma \bar{p} / \bar{\rho}}$ is the velocity of sound in steady state, then \bar{v} can be neglected. For details see "Dimensionless Quantities." Setting $\bar{v} = 0$ leads to the dynamics of (10) being decoupled: the density $\tilde{\rho}$ does not couple into the pressure and velocity dynamics and can be dropped from consideration. Therefore, the linearization of the gas dynamics yields the following wave equation with the heat fluctuations \tilde{Q} as a source term at $x = x_0$

$$\frac{\partial}{\partial t} \begin{bmatrix} \tilde{v} \\ \tilde{p} \end{bmatrix} = \begin{bmatrix} 0 & -\frac{1}{\tilde{\rho}} \\ -\gamma \tilde{p} & 0 \end{bmatrix} \frac{\partial}{\partial x} \begin{bmatrix} \tilde{v} \\ \tilde{p} \end{bmatrix} + \begin{bmatrix} 0 \\ \tilde{\gamma} \end{bmatrix} \delta(x - x_0) \tilde{Q}(t). \quad (11)$$

The boundary conditions (6) on pressure and the speaker signal u can be written in the general form

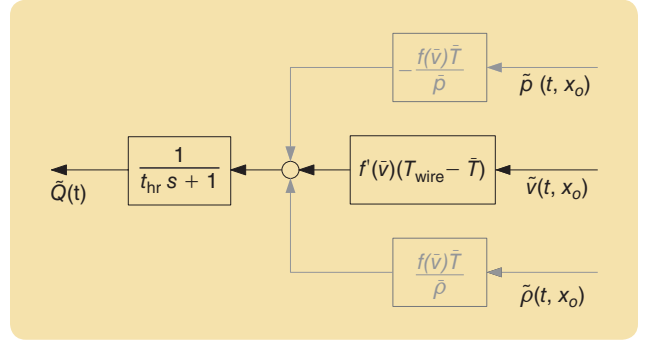


FIGURE 17 A signal flow diagram of the linearized heat-release model. The analysis in "Dimensionless Quantities" shows that the gains of the local acoustic pressure $\tilde{p}(t, x_0)$ and the local density variation $\tilde{\rho}(t, x_0)$ are much smaller than the gain of the local acoustic velocity $\tilde{v}(t, x_0)$, hence they may be neglected.

$$\begin{bmatrix} 1 \\ 0 \end{bmatrix} u(t) = \begin{bmatrix} 0 & 1 \\ 0 & 0 \end{bmatrix} \begin{bmatrix} \tilde{v}(t,0) \\ \tilde{p}(t,0) \end{bmatrix} + \begin{bmatrix} 0 & 0 \\ 0 & 1 \end{bmatrix} \begin{bmatrix} \tilde{v}(t,L) \\ \tilde{p}(t,L) \end{bmatrix}. \quad (12)$$

The two equations (11) and (12) represent the LTI dynamics of acoustics driven by the two scalar inputs $\tilde{Q}(t)$ and $u(t)$. The remaining task is to find an expression for the transfer functions from those two inputs to the pressure and velocity at any location within the tube as outputs. A standard technique is to apply the Laplace transform to (11) and (12) and rearrange so that the spatial derivative is on the left-hand side of the equation. The result is an ordinary differential equation (ODE) with boundary conditions

$$\begin{bmatrix} \mathcal{V}'(s,x) \\ \mathcal{P}'(s,x) \end{bmatrix} = \begin{bmatrix} 0 & \frac{-s}{\gamma \tilde{p}} \\ -s \tilde{\rho} & 0 \end{bmatrix} \begin{bmatrix} \mathcal{V}(s,x) \\ \mathcal{P}(s,x) \end{bmatrix} + \begin{bmatrix} \frac{\tilde{\gamma}}{\tilde{p} A} \\ 0 \end{bmatrix} \delta(x - x_0) \mathcal{Q}(s) \\ \begin{bmatrix} 1 \\ 0 \end{bmatrix} \mathcal{U}(s) = \begin{bmatrix} 0 & 1 \\ 0 & 0 \end{bmatrix} \begin{bmatrix} \mathcal{V}(s,0) \\ \mathcal{P}(s,0) \end{bmatrix} + \begin{bmatrix} 0 & 0 \\ 0 & 1 \end{bmatrix} \begin{bmatrix} \mathcal{V}(s,L) \\ \mathcal{P}(s,L) \end{bmatrix}, \quad (13)$$

where $\mathcal{V}(s,x)$, $\mathcal{P}(s,x)$, $\mathcal{U}(s)$, and $\mathcal{Q}(s)$ are the Laplace transforms (in t) of $\tilde{v}(t,x)$, $\tilde{p}(t,x)$, $u(t)$, and $\tilde{Q}(t)$, respectively, and differentiation in x is denoted by prime, for example, $\mathcal{V}'(s,x) = d/dx \mathcal{V}(s,x)$. The Laplace transform variable s can be simply regarded as a parameter in the above differential equation, which can now be treated as an ODE (in x) with two point boundary conditions. A general formula (S7) for the solution of this two-point boundary-value problem is derived in "Transfer Function Computation for Two-Point Boundary Value Problems." Application of this procedure to (13) yields the transfer function matrix (3).

Linearization of the Heat Release

To facilitate interconnection of heat release and acoustic models, the temperature T in King's law (9b) can be expressed in terms of the state variables of acoustics p and ρ by using the ideal gas law $T = p / (\rho R)$; note that now, T_{gas} is not initially assumed to be constant, but it is shown in

“Dimensionless Quantities” that its contribution (expressed with pressure and density) can be neglected. As in the preceding section, all variables are then expressed as steady state plus deviation, for example, $v = \bar{v} + \tilde{v}$, and the linearized version of (9b) takes the three-input form

$$\tilde{Q}_K = \begin{bmatrix} f(\bar{v}) \frac{\bar{T}}{\bar{\rho}} & f'(\bar{v})(T_{\text{wire}} - \bar{T}) & -f(\bar{v}) \frac{\bar{T}}{\bar{p}} \end{bmatrix} \begin{bmatrix} \tilde{\rho} \\ \tilde{v} \\ \tilde{p} \end{bmatrix}, \quad (14)$$

conveniently written as a vector gain multiplying the acoustic states. $\bar{T} = \bar{p}/(\bar{\rho}R)$ is the steady-state temperature and simply a parameter, and $f(v) = l_w(\kappa + \kappa_v \sqrt{|v|})$ is the velocity-dependent heat transfer coefficient according to King’s law (8).

This representation of the heat release dynamics illustrates nicely that while all three state variables influence the heat transfer process, they do so with different gains, and so it is no surprise that this model can also be simplified

substantially by considering the relative sizes of those gains. Careful dimensional analysis of the linearization shows velocity fluctuations to be the main driver of heat release dynamics when the flow is very subsonic (that is, $\bar{v} \ll c$); for details, see “Dimensionless Quantities.” It is thus reasonable to proceed with the single-input linearized version of (9b)

$$\tilde{Q}_K = f'(\bar{v})(T_s - \bar{T})\tilde{v}.$$

Figure 17 depicts this reduction graphically. For the range of steady velocities \bar{v} in the Rijke tube experiment, the nonlinear heat release dynamics (the bottom loop of Figure 15) are only a function of velocity fluctuations, and the linearization is represented compactly by the transfer function

$$B(s) = \frac{f'(\bar{v})(T_s - \bar{T})}{t_{\text{hr}}s + 1} \quad (15)$$

Dimensionless Quantities

It is common practice in fields such as fluid dynamics or heat transfer to express physical relationships in terms of dimensionless quantities, and for good reasons: it often leads to a reduced number of parameters, allows comparing relative sizes more easily, and leads to aesthetically more appealing equations.

In the model equations for the Rijke tube, there are three dependent variables, namely ρ , v , and p , and the two independent variables x and t . Variables are nondimensionalized by setting them in relation to some reference value; a natural reference value for the pressure p would be its nominal value, the atmospheric pressure $p_0 = \bar{p}$, similarly for ρ . The situation is different for the velocity v . It is expected that the nominal velocity \bar{v} is very small, hence scaling v by \bar{v} would lead to a large quantity, not comparable to the scaled pressure and density. In other words, while the percentage change in p and ρ will be small, the percentage change in v will be large. Thus, the velocity is scaled by c , the speed of sound, and the set of scaled variables is

$$\psi := \rho/\bar{\rho}, \quad m := v/c, \quad \text{and} \quad r := p/\bar{p}.$$

Similarly, scaling the spatial variable x by the tube length L and time t by the time it takes sound to propagate through the entire tube yields

$$\xi := x/L, \quad \tau := ct/L,$$

and

$$\frac{\partial}{\partial \xi} = L \frac{\partial}{\partial x}, \quad \frac{\partial}{\partial \tau} = \frac{L}{c} \frac{\partial}{\partial t}.$$

Rewriting, for example, the conservation of momentum equation (see Table S1) using dimensionless variables and the relation $c^2 = \gamma\bar{p}/\bar{\rho}$ leads to

$$\frac{\partial m}{\partial \tau} = -m \frac{\partial m}{\partial \xi} - \frac{1}{\gamma r} \frac{\partial \psi}{\partial \xi}.$$

Rewriting the state-space model (10) in terms of the dimensionless variables yields the more appealing dimensionless form

$$\frac{\partial}{\partial \tau} \begin{bmatrix} \tilde{r} \\ \tilde{m} \\ \tilde{\psi} \end{bmatrix} = - \begin{bmatrix} \text{Ma} & 1 & 0 \\ 0 & \text{Ma} & \frac{1}{\gamma} \\ 0 & \gamma & \text{Ma} \end{bmatrix} \frac{\partial}{\partial \xi} \begin{bmatrix} \tilde{r} \\ \tilde{m} \\ \tilde{\psi} \end{bmatrix} + \begin{bmatrix} 0 \\ 0 \\ \dot{q} \end{bmatrix}, \quad (S1)$$

where $\tilde{\cdot}$ signifies deviation from steady state, $\text{Ma} := \bar{v}/c$ is the Mach number, and $\dot{q} := (\bar{\gamma}L/\bar{\rho}c)q$ simply lumps q with several parameters to obtain a dimensionless input.

Using (S1), the case for neglecting the diagonal elements in (10) can now be made more rigorous: without computation or measurement, it is clear that $\text{Ma} \ll 1$, whereas γ is of order unity, hence compared to γ , $\text{Ma} \approx 0$.

Similarly, rewriting (14) using the dimensionless variables gives

$$\tilde{Q}_K = \begin{bmatrix} f(\bar{v})\bar{T} & cf'(\bar{v})(T_{\text{wire}} - \bar{T}) & -f(\bar{v})\bar{T} \end{bmatrix} \begin{bmatrix} \tilde{r} \\ \tilde{m} \\ \tilde{\psi} \end{bmatrix}.$$

A comparison of the gains of \tilde{r} and $\tilde{\psi}$, on the one hand, and \tilde{m} , on the other, leads to

$$\frac{f(\bar{v})\bar{T}}{cf'(\bar{v})(T_{\text{wire}} - \bar{T})} = 2 \frac{\bar{T}}{(T_{\text{wire}} - \bar{T})} \left(\frac{\kappa}{\kappa_v \sqrt{\bar{v}}} + 1 \right) \text{Ma}.$$

If all terms except for Ma can be expected to be of order unity or less, then it is justified to neglect the contributions of density and pressure variations to the heat transfer. The only term in question is $\kappa/(\kappa_v \sqrt{\bar{v}})$ the ratio between conductive and convective heat transfer; these are typically comparable (see [20, Tables V, VI] and note that velocities are measured in cm/s), and hence this term is also of order unity.

This experiment is perhaps the simplest illustration of the phenomenon of thermoacoustic instabilities.

between local velocity fluctuations $\tilde{v}(t, x_o)$ and heat released into the gas $\tilde{Q}(t)$; see also Figures 14 and 17.

It should be stressed here that the significance of the steady buoyancy-induced upward velocity \bar{v} is very different for the heat release than for the gas dynamics. The wave-like equation (11) for the gas dynamics was obtained by assuming $\bar{v} \approx 0$ with the justification that the dynamics would not change much if \bar{v} were nonzero but small. For the heat transfer, however, assuming no steady upward component in the velocity would result in an invalid linearization, since the derivative of $\sqrt{|\cdot|}$ is discontinuous at zero. The importance of the offset in velocity lies in moving to the “linearizable part” of the square root function, as depicted in the bottom block in Figure 15.

Comparison of Modeling and Empirical Results

Finally, the previous modeling efforts can be used to test how closely the physical model (3) corresponds to reality (or rather the identified model as a proxy for reality) beyond explaining the thermoacoustic oscillations. It is important to understand first the relationship between the modeled and identified transfer functions. The open-loop Bode plot of Figure 8 corresponds to the identified response $F(e^{j\omega})$ of pressure fluctuations, as measured by the microphone, to pressure fluctuations induced by the speaker. In the model depicted in Figure 15, this Bode plot would correspond to the transfer function from $\tilde{p}(0)$ to $\tilde{p}(x_m)$ (with w and K set to zero), including the (linearized) heat release feedback loop. For clarity, this is illustrated in Figure 18. (The identified response F also includes dynamics of the audio components; see Figure 5. By neglecting them in the modeling process, it is implicitly assumed that those components can be modeled as pure gains, and this assumption is justified, since the frequency range of interest is well within the audible range of human hearing.)

Comparisons need to be made between the identified open loop $F(e^{j\omega})$ and

$$\check{F}(s) = G_{11}(s) + \frac{G_{12}(s)B(s)G_{21}(s)}{1 - G_{22}(s)B(s)}.$$

There remain, however, several unknown parameters in the model: an overall gain due to the unknown conversion factors of speaker and microphone, the microphone position x_m , and the linear gain and time constant t_{hr} of the heat-release feedback $B(s)$. Additionally, the assumptions about friction, diffusive effects, and the steady upward flow that were made during the modeling of the gas dynamics, because they lead to a very simple model (11)

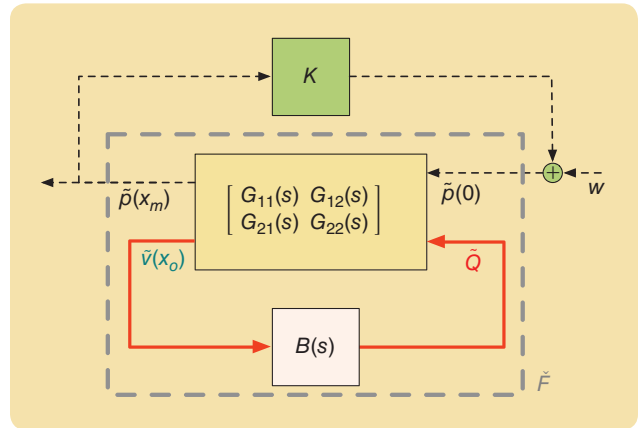


FIGURE 18 The modeled transfer function between speaker input and microphone output signals can be represented—with linearized heat release—as a lower linear fractional transformation $\check{F} = G_{11} + G_{12}BG_{21}/(1 - G_{22}B)$.

and transfer function (3), also lead to system poles moving onto the imaginary axis, which made necessary the less-than-rigorous argument that, intuitively, the neglected damping would move the poles toward the left (rendering them stable) and presents a clinical case that makes comparisons difficult. “Wave Dynamics with Diffusion and

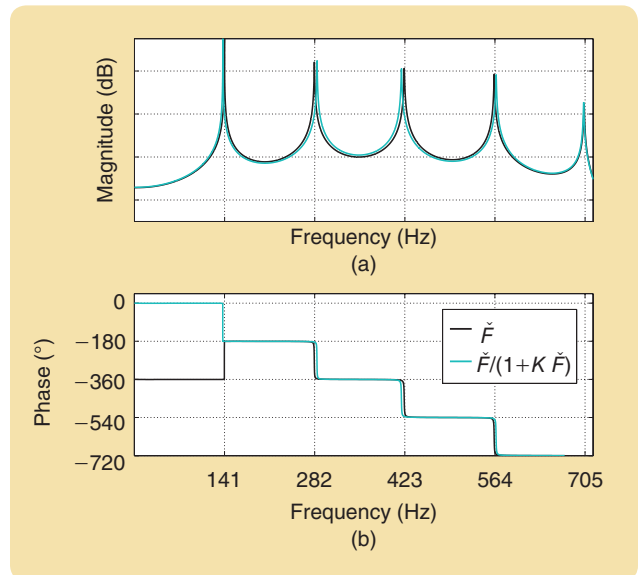


FIGURE 19 Bode plots of open-loop ($K = 0$) and closed-loop (with a stabilizing $K \neq 0$) frequency responses derived from the physical model of Figures 18 and 14. Note the opposite signs of the 180° phase increase near the fundamental mode indicating open-loop instability and closed-loop stability of that mode.

The root locus explains why proportional feedback initially stabilizes the thermoacoustic instability and why a higher-frequency mode becomes unstable at high gains.

Damping” addresses the issue numerically, and Figure S6 suggests that the poles lie on a parabola shape.

If the damping effect is imitated by considering $j\omega + \varepsilon_0 + \varepsilon_1\omega^2$ instead of $j\omega$, and choices of the unknown heat release time constant, heat-release gain, and feedback gain are made judiciously, the responses shown in Figure 19 are obtained. Remarkably, despite employing very simple devices to treat the aforementioned difficulties, these responses qualitatively capture the most important features of Figures 6 and 7: resonant peaks, a phase increase of 180° at the first peak for the unstabilized open loop \dot{F} , and phase drops of the same amount at the higher-order peaks for \dot{F} and at all peaks for the stabilized closed loop $\dot{F}/(1 + K\dot{F})$. That it is easy to find a wide range of parameter values that generate responses with these features after only a few manual iterations can be seen as evidence that the physical model indeed captures the important structures of the underlying physics.

SUMMARY

The Rijke tube experiment has been presented from a control engineer’s perspective. To emphasize this perspective, the first part of the article showed how the experiment can be approached using “black box” techniques, such as system identification and model validation. Although a great deal of insight can be obtained from these generic systems techniques, a thorough understanding of the underlying dynamics is achieved by physical modeling from first principles in the second part of the article. As is typical in any control-oriented modeling exercise, choices must be made as to the right level of “granularity” of various pieces of the model. In this article, these choices were guided by the findings in the empirical part of the investigation. A notable example is modeling the boundary-layer effect on heat release from the coil, without which the root locus arguments presented would fail to explain the observed limit cycle frequencies in the experiment. While a full-fidelity model of that boundary layer would be rather complex, it was shown that a first-order lag model for that boundary layer is sufficient to produce consistent predictions. This back-and-forth cross validation between modeling and experiment can serve as an instructive pedagogical device.

Thermoacoustic effects are mostly known within the control community as undesirable phenomena that need to be regulated [2], [23], [3], [24]–[26], [6], [27]. There is, however, another perspective in which these effects can be regarded as an *energy conversion* mechanism. In the Rijke

tube, the thermoacoustic instability produces a limit cycle that can be thought of as a mechanism for converting some of the steady heater power into acoustic power radiated from the tube. This is only one example of several types of thermoacoustic engines in which powerful, internally contained acoustic waves perform the mechanical work in the energy conversion process [28], [29]. Thus, acoustic waves replace the traditional pistons, cranks, and turbines typically used in traditional heat engines and can therefore potentially have very high efficiencies. With some notable exceptions [30]–[32], these devices have not received much attention from control engineers. Although the Rijke tube is not a useful heat engine, the underlying energy conversion mechanisms are sufficiently similar to thermoacoustic engines to render it a simple and useful experimental test bed for active control of thermoacoustic phenomena.

ACKNOWLEDGMENT

This work was partially supported by NSF awards CMMI-1363386 and ECCS-1408442.

AUTHOR INFORMATION

Jonathan P. Epperlein (jpe@engineering.ucsb.edu) was awarded the Dipl.-Ing. degree in engineering cybernetics from Otto-von-Guericke Universität, Magdeburg, Germany, in 2008 and the M.Sc. in electrical and computer engineering from the University of California, Santa Barbara, in 2011, where he is currently pursuing a Ph.D. degree. He has also spent time at the Hamilton Institute in Maynooth, Ireland, Yale University, and Harvard Medical School. His current research interests include modeling and control of thermoacoustic systems, spatially invariant distributed-parameter systems, and optimal periodic control. He can be contacted at the Department of Mechanical Engineering, Building Eng. II, Room 2355, University of California, Santa Barbara, Santa Barbara, CA 93106-5070 USA.

Bassam Bamieh is a professor of mechanical engineering and associate director of the Center for Control, Dynamical Systems, and Computation at the University of California, Santa Barbara (UCSB). He received the B.Sc. degree in electrical engineering and physics from Valparaiso University, Indiana, in 1983 and the M.Sc. and Ph.D. degrees in electrical and computer engineering from Rice University, Houston, Texas, in 1986 and 1992, respectively. Prior to joining UCSB in 1998, he was an assistant professor in the Department of Electrical and Computer Engineering and

the Coordinated Science Laboratory at the University of Illinois at Urbana-Champaign (1991–1998). His research interests are in robust and optimal control; spatially distributed systems; and problems at the interface between control, fluid mechanics, and statistical physics. He is a past recipient of the IEEE Control Systems Society G.S. Axelby Outstanding Paper Award (twice), the AACC Hugo Schuck Best Paper Award, and a National Science Foundation CAREER award. He was elected a Distinguished Lecturer of the IEEE Control Systems Society (2005) and a Fellow of IEEE and the International Federation of Automatic Control.

Karl J. Åström was educated at The Royal Institute of Technology (KTH) in Stockholm. During his studies, he worked on inertial navigation for Swedish defense agencies. He joined IBM in 1961 to work on computer control. In 1965 he was appointed professor of the new chair of automatic control at Lund Institute of Technology/Lund University, where he established a new department. From 2000 to 2009 he was professor of mechanical engineering at the University of California, Santa Barbara. He is now senior professor at Lund University. He has broad interests in control, has an Erdős number of 3, and is a Life Fellow of IEEE. He has been awarded many honors, including the 1985 ASME Rufus Oldenburger medal, the 1987 Quazza Medal from IFAC, the 1990 IEEE Control Systems Award, and the 1993 IEEE Medal of Honor. He is a member of the Royal Swedish Academy of Science, the Royal Swedish Academy of Engineering Science, and the U.S. National Academy of Engineering.

REFERENCES

- [1] P. L. Rijke, "Über eine neue Art, die in einer an beiden Enden offenen Röhre enthaltene Luft in Schwingungen zu versetzen," *Annalen der Physik*, vol. 183, no. 6, pp. 339–343, 1859.
- [2] J. Hathout, A. Annaswamy, M. Fleifil, and A. Ghoniem, "A model-based active control design for thermoacoustic instability," *Comb. Sci. Technol.*, vol. 132, no. 1, pp. 99–138, 1998.
- [3] A. Annaswamy, M. Fleifil, J. Rumsey, R. Prasanth, J. Hathout, and A. Ghoniem, "Thermoacoustic instability: Model-based optimal control designs and experimental validation," *IEEE Trans. Control Syst. Technol.*, vol. 8, no. 6, pp. 905–918, 2000.
- [4] A. McIntosh, "Flame resonance and acoustics in the presence of heat loss," *Lect. Appl. Maths*, vol. 24, pt. 1, pp. 269–301, 1986.
- [5] A. McIntosh, "On flame resonance in tubes," *Comb. Sci. Technol.*, vol. 69, nos. 4–6, pp. 147–152, 1990.
- [6] A. P. Dowling and A. S. Morgans, "Feedback control of combustion oscillations," *Annu. Rev. Fluid Mech.*, vol. 37, pp. 151–182, Jan. 2005.
- [7] M. Juniper, "Triggering in the horizontal Rijke tube: Non-normality, transient growth and bypass transition," *J. Fluid Mech.*, vol. 667, pp. 272–308, Jan. 2011.
- [8] M. Heckl and M. Howe, "Stability analysis of the Rijke tube with a Green's function approach," *J. Sound Vib.*, vol. 305, nos. 4–5, pp. 672–688, 2007.
- [9] R. Raun, M. Beckstead, J. Finlanson, and K. Brooks, "A review of Rijke tubes, Rijke burners and related devices," *Progr. Energy Comb. Sci.*, vol. 19, no. 4, pp. 313–364, 1993.
- [10] H. Levine and J. Schwinger. (1948, Feb.). On the radiation of sound from an unflanged circular pipe. *Phys. Rev.* [Online]. 73, pp. 383–406. Available: <http://link.aps.org/doi/10.1103/PhysRev.73.383>
- [11] I. Gustavsson, L. Ljung, and T. Söderström, "Identification of processes in closed loop—Identifiability and accuracy aspects," *Automatica*, vol. 13, no. 1, pp. 59–75, 1977.
- [12] U. Forsell and L. Ljung, "Closed-loop identification revisited," *Automatica*, vol. 35, no. 7, pp. 1215–1241, 1999.
- [13] A. S. Morgans and A. P. Dowling. (2007). Model-based control of combustion instabilities. *J. Sound Vib.* [Online]. 299(1–2), pp. 261–282. Available: <http://www.sciencedirect.com/science/article/pii/S0022460X06006079>
- [14] S. J. Illingworth, A. S. Morgans, and C. W. Rowley. (2011). Feedback control of flow resonances using balanced reduced-order models. *J. Sound Vib.* [Online]. 330(8), pp. 1567–1581. Available: <http://www.sciencedirect.com/science/article/pii/S0022460X10007169>
- [15] L. Ljung, *System Identification: Theory for the User*. Upper Saddle River, NJ: PTR Prentice Hall, 1999.
- [16] L. Ljung, "System identification toolbox for use with MATLAB," MathWorks Inc., Natick, MA, 2007.
- [17] R. de Callafon and P. M. van den Hof, "FREQID—Frequency domain identification toolbox for use with MATLAB," *Select. Topics Identif. Model. Control*, vol. 9, pp. 129–134, Dec. 1996.
- [18] D. Bayard, "Statistical plant set estimation using Schroeder-phased multisinusoidal input design," *Appl. Math. Comput.*, vol. 58, no. 2, pp. 169–198, 1993.
- [19] J. Burgess, "Chirp design for acoustical system identification," *J. Acoust. Soc. Amer.*, vol. 91, no. 3, p. 1525, 1992.
- [20] L. V. King, "On the convection of heat from small cylinders in a stream of fluid: Determination of the convection constants of small platinum wires with applications to hot-wire anemometry," *Philos. Trans. Royal Soc.*, vol. 214, pp. 373–432, 1914.
- [21] A. P. Dowling, "Nonlinear self-excited oscillations of a ducted flame," *J. Fluid Mech.*, vol. 346, pp. 271–290, Sept. 1997.
- [22] N. Olgac, R. Cepega-Gomez, U. Zalluhoglu, and A. S. Kammer, "An unconventional perspective in thermoacoustic instability using a novel mathematical tool," Dept. Mech. Eng., Univ. Connecticut, Storrs, CT, Tech. Rep., 2013.
- [23] A. Banaszuk, K. B. Ariyur, M. Krstić, and C. A. Jacobson, "An adaptive algorithm for control of combustion instability," *Automatica*, vol. 40, no. 11, pp. 1965–1972, 2004.
- [24] J. E. Tierno and J. C. Doyle, "Multimode active stabilization of a Rijke tube," in *Proc. ASME Winter Annu. Meeting Active Control Noise Vibration*, 1992, vol. 38, pp. 65–68.
- [25] B. Zinn and Y. Neumeier, "An overview of active control of combustion instabilities," in *Proc. 35th Aerospace Sciences Meeting Exhibit*, 1997, vol. 461, paper no. 97-0461.
- [26] S. Candel, "Combustion dynamics and control: Progress and challenges," *Proc. Combust. Inst.*, vol. 29, no. 1, pp. 1–28, 2002.
- [27] M. Heckl, "Active control of the noise from a Rijke tube," *J. Sound Vib.*, vol. 124, no. 1, pp. 117–133, 1988.
- [28] S. Garrett and S. Backhaus, "The power of sound," *Amer. Sci.*, vol. 88, no. 6, p. 516, 2000.
- [29] H. Madarame, "Thermally induced acoustic oscillations in a pipe. I—Oscillations induced by plane heat source in air current," *JSME Int. J. Ser. B*, vol. 24, pp. 1626–1633, Sept. 1981.
- [30] Y. Li, B. L. Minner, G. T.-C. Chiu, L. Mongeau, and J. E. Braun, "Adaptive tuning of an electrodynamically driven thermoacoustic cooler," *J. Acoust. Soc. Amer.*, vol. 111, no. 3, pp. 1251–1258, 2002.
- [31] Y. Li, G. T.-C. Chiu, and L. Mongeau, "Dual-driver standing wave tube: Acoustic impedance matching with robust repetitive control," *IEEE Trans. Control Syst. Technol.*, vol. 12, no. 6, pp. 869–880, 2004.
- [32] Y. Li, M. A. Rotea, G. T.-C. Chiu, L. Mongeau, and I.-S. Paek, "Extremum seeking control of a tunable thermoacoustic cooler," *IEEE Trans. Control Syst. Technol.*, vol. 13, no. 4, pp. 527–536, July 2005.
- [33] M. J. Lighthill, "The response of laminar skin friction and heat transfer to fluctuations in the stream velocity," *Proc. Royal Soc. London A, Math. Phys. Sci.*, vol. 224, no. 1156, pp. 1–23, 1954.
- [34] J. P. Epperlein, "Topics in modeling and control of spatially distributed systems," Ph.D. dissertation, Univ. California, Santa Barbara, CA, Dec. 2014.
- [35] L. N. Trefethen. (2000). Spectral methods in MATLAB. *Soc. Ind. Appl. Math.* [Online]. Available: <http://epubs.siam.org/doi/abs/10.1137/1.9780898719598>

